

THE SEGUE STELLAR PARAMETER PIPELINE. I. DESCRIPTION AND COMPARISON OF INDIVIDUAL METHODS

YOUNG SUN LEE¹, TIMOTHY C. BEERS¹, THIRUPATHI SIVARANI¹, CARLOS ALLENDE PRIETO², LARS KOESTERKE^{2,11}, RONALD WILHELM³, PAOLA RE FIORENTIN^{4,12}, CORYN A. L. BAILER-JONES⁴, JOHN E. NORRIS⁵, CONSTANCE M. ROCKOSI⁶, BRIAN YANNY⁷, HEIDI J. NEWBERG⁸, KEVIN R. COVEY⁹, HAO-TONG ZHANG¹⁰, AND A.-LI LUO¹⁰

¹ Department of Physics & Astronomy, CSCE: Center for the Study of Cosmic Evolution, and Joint Institute for Nuclear Astrophysics, Michigan State University, East Lansing, MI 48824, USA; lee@pa.msu.edu, beers@pa.msu.edu, thirupathi@pa.msu.edu

² Department of Astronomy, University of Texas, Austin, TX 78712, USA; callende@astro.as.utexas.edu

³ Department of Physics, Texas Tech University, Lubbock, TX 79409, USA; ron.wilhelm@ttu.edu

⁴ Max-Planck-Institute für Astronomie, Königstuhl 17, D-69117, Heidelberg, Germany; fiorent@mpia-hd.mpg.de, calj@mpia-hd.mpg.de
⁵ Research School of Astronomy and Astrophysics, The Australian National University, Weston, ACT 2611, Australia; jen@mso.anu.edu.au

⁶ Department of Astronomy, University of California, Santa Cruz, CA 95064, USA; crockosi@ucolick.org

⁷ Fermi National Accelerator Laboratory, Batavia, IL 60510, USA; yanny@fnal.gov

⁸ Department of Physics & Astronomy, Rensselaer Polytechnical Institute, Troy, NY 12180, USA; newbeh@rpi.edu

⁹ Harvard-Smithsonian Center for Astrophysics, 60 Garden Street, Cambridge, MA 02138, USA; kcovey@cfa.harvard.edu

¹⁰ National Astronomical Observatories of China, Chinese Academy of Sciences, Beijing 100012, China; zht@lamost.org, lal@lamost.org

Received 2007 October 31; accepted 2008 August 17; published 2008 October 13

ABSTRACT

We describe the development and implementation of the Sloan Extension for Galactic Exploration and Understanding (SEGUE) Stellar Parameter Pipeline (SSPP). The SSPP is derived, using multiple techniques, radial velocities, and the fundamental stellar atmospheric parameters (effective temperature, surface gravity, and metallicity) for AFGK-type stars, based on medium-resolution spectroscopy and *ugriz* photometry obtained during the course of the original Sloan Digital Sky Survey (SDSS-I) and its Galactic extension (SDSS-II/SEGUE). The SSPP also provides spectral classification for a much wider range of stars, including stars with temperatures outside the window where atmospheric parameters can be estimated with the current approaches. This is Paper I in a series of papers on the SSPP; it provides an overview of the SSPP, and tests of its performance using several external data sets. Random and systematic errors are critically examined for the current version of the SSPP, which has been used for the sixth public data release of the SDSS (DR-6).

Key words: methods: data analysis – stars: abundances – stars: fundamental parameters – surveys – techniques: spectroscopic

1. INTRODUCTION

The Sloan Extension for Galactic Understanding and Exploration (SEGUE) is one of the three surveys that were executed as part of the first extension of the Sloan Digital Sky Survey (SDSS-II), which comprises the subsurveys LEGACY, SUPERNOVA SURVEY, and SEGUE. The SEGUE program was designed, in part, to obtain *ugriz* imaging of some 3500 deg² of sky outside of the original SDSS-I footprint (Fukugita et al. 1996; Gunn et al. 1998, 2006; York et al. 2000; Stoughton et al. 2002; Abazajian et al. 2003, 2004, 2005; Pier et al. 2003; Adelman-McCarthy et al. 2006, 2007, 2008). The regions of sky targeted were primarily at lower Galactic latitudes ($|b| < 35^\circ$), in order to better sample the disk/halo interface of the Milky Way. As of Data Release 6 (DR-6, Adelman-McCarthy et al. 2008), about 85% of the planned additional imaging had been completed. SEGUE also obtained $R \simeq 2000$ spectroscopy over the wavelength range 3800–9200 Å, for some 250,000 stars in 200 selected areas over the sky available from Apache Point, New Mexico. The spectroscopic candidates were selected on the basis of *ugriz* photometry to populate 14 target categories (see Table 2 in Adelman-McCarthy et al. 2008 for the target-selection algorithms employed), chosen to explore the nature of the Galactic stellar populations at distances from

0.5 kpc to over 100 kpc from the Sun. The SEGUE data clearly require automated analysis tools in order to efficiently extract the maximum amount of useful astrophysical information for the targeted stars, in particular their stellar atmospheric parameters, over wide ranges of effective temperature (T_{eff}), surface gravity ($\log g$), and metallicity ([Fe/H]).

Numerous methods have been developed in the past in order to extract atmospheric-parameter estimates from medium-resolution stellar spectra in a fast, efficient, and automated fashion. These approaches include techniques for finding the minimum distance (parameterized in various ways) between observed spectra and grids of synthetic spectra (e.g., Allende Prieto et al. 2006), nonlinear regression models (e.g., Re Fiorentin et al. 2007, and references therein), correlations between broadband colors and the strength of prominent metallic lines, such as the Ca II K line (Beers et al. 1999), autocorrelation analysis of a stellar spectrum (Beers et al. 1999, and references therein), obtaining fits of spectral lines (or summed line indices) as a function of broadband colors (Wilhelm et al. 1999), or the behavior of the Ca II triplet lines as a function of broadband color (Cenarro et al. 2001a, 2001b). Each of these approaches exhibits optimal behavior over restricted temperature and metallicity ranges; outside of these regions they are often uncalibrated, suffer from saturation of the metallic lines used in their estimates at high metallicity or low temperatures, or lose efficacy due to the weakening of metallic species at low metallicity or high temperatures. The methods that make use of specific spectral features are susceptible to other problems, e.g., the presence of

¹¹ Current address: Texas Advanced Computer Center, The University of Texas, Austin, TX 78758, USA.

¹² Current address: Department of Physics, University of Ljubljana, Jadranska 19, 1000 Ljubljana, Slovenia.

emission in the core of the Ca II K line for chromospherically active stars, or poor telluric line subtraction in the region of the Ca II triplet. Because SDSS stellar spectra cover most of the entire optical wavelength range, one can apply several approaches, using different wavelength regions, in order to glean optimal information on stellar parameters. The combination of multiple techniques results in estimates of stellar parameters that are more robust over a much wider range of T_{eff} , $\log g$, and [Fe/H] than those that might be produced by individual methods.

In this first paper of a series, we describe the SEGUE Stellar Parameter Pipeline (hereafter, SSPP), which implements this “multimethod” philosophy. We also carry out a number of tests to assess the range of stellar atmospheric parameter space over which the estimates obtained by the SSPP remain valid. The second paper in the SSPP series (Lee et al. 2008; hereafter Paper II) seeks to validate the radial velocities and stellar parameters determined by the SSPP by comparison with selected member stars of three globular clusters (M 15, M 13, and M 2) and two open clusters (NGC 2420 and M 67). A comparison with an analysis of high-resolution spectra for SDSS-I/SEGUE stars is presented in the third paper in this series (Allende Prieto et al. 2008; hereafter Paper III).

In the following, the colors ($u - g$, $g - r$, $r - i$, $i - z$, and $B - V$) and magnitudes (u , g , r , i , z , B , and V) are understood to be de-reddened and corrected for absorption (using the dust maps of Schlegel et al. 1998), unless stated specifically otherwise.

2. DETERMINATION OF RADIAL VELOCITIES

2.1. The Adopted Radial Velocity Used by the SSPP

The *spZ* best fits file, which is generated from the SDSS spectroscopic reduction pipeline (Stoughton et al. 2002), provides two estimated radial velocities. One is an absorption-(or emission-) line redshift computed from a cross-correlation procedure using templates that were obtained from SDSS commissioning spectra (Stoughton et al. 2002)—the *spectro1d* redshifts. Another estimate comes from performing a “best-match” procedure that compares the observed spectra with externally measured templates (in this case, the ELODIE library of high-resolution spectra, as described by Prugniel & Soubiran 2001), degraded to match the resolving power of SDSS spectra (Adelman-McCarthy et al. 2008).

Previous experience with the analysis of SDSS stellar spectra suggested that the radial velocity estimated from the ELODIE template matches is often the best available estimate, in the sense that it is the most repeatable, based on the spectra of “quality assurance” stars with multiple determinations. In addition, the *spectro1d* redshifts exhibit larger systematic offsets, as high as 12 km s⁻¹ (Adelman-McCarthy et al. 2008). Hence, as a first choice, we adopt the radial velocity from the ELODIE template matches and set the radial-velocity indicator flag to “ELRV.” However, there are some cases where the velocities from the ELODIE template matches are not reported, because an adequate match to the (somewhat incomplete) ELODIE library could not be made with confidence. In such cases, we check the *spectro1d* redshifts; if a velocity is reported by this routine, we adopt it, and the radial-velocity flag is set to “BSRV.”

If neither of the above two velocities are reported, which happens only rarely, and mainly for quite low signal-to-noise ratio (S/N; $<5/1$) spectra, then we obtain an independent estimate of the radial velocity based on our own IDL routines.

The calculation of this radial-velocity estimate is carried out by determining wavelength shifts for several strong absorption line features (Ca II K, Ca II H, H δ , Ca I, H γ , H β , Na I, H α , and the Ca II triplet). After ignoring any likely spurious values (calculated velocity above +500 km s⁻¹ or below -500 km s⁻¹) from the individual lines, we obtain a 3 σ -clipped average of the remaining radial velocities. If this computed average falls between -500 km s⁻¹ and +500 km s⁻¹, we take the calculated radial velocity as the adopted radial velocity, and set the radial-velocity flag to “CALRV.” We have noted that certain types of stars, in particular cool stars with large carbon enhancements, present a challenge for the radial-velocity estimates adopted by the SSPP. We have developed new carbon-enhanced templates, based on synthetic spectra, which appear to return improved estimates. These will be implemented in the next version of the SDSS spectroscopic reduction pipeline, which we anticipate applying for the final SDSS-II data release, DR-7.

It should be noted that many of the techniques used for atmospheric-parameter estimation in the SSPP work well even when the velocity determination for a given star has errors of up to 100 km s⁻¹ or more. Table 1, which summarizes an experiment on how the derived atmospheric parameters change as a result of systematically shifting the radial-velocity estimate by 50, 100, 150, and 200 km s⁻¹ relative to the original value, confirms this. We made use of 125 SDSS-I/SEGUE high-resolution calibration stars (obtained with the Hobby-Eberly Telescope (HET), see Paper III), all of which have well-determined stellar parameters, thanks to their high quality (S/N $> 50/1$). See Sections 4 and 5 for the naming convention and the description of each parameter estimation method. As can be seen in Table 1, most of the methods suffer zero-point shifts in $\log g$ and [Fe/H] less than 0.1 dex, with a scatter of below 0.2 dex, even for radial-velocity shifts as high as 100 km s⁻¹. This level of scatter is on the order of the typical uncertainty (~ 0.2 –0.3 dex) for these parameters obtained from our analysis of medium-resolution spectra in the SDSS. The reason for the lack of significant scatter is that many of our methods compare with synthetic spectra over wide spectral ranges, rather than by a line-by-line comparison to weak individual lines, to determine the stellar parameters. Even for those techniques that employ line-index approaches, the SSPP employs relatively wide bandwidths, which mitigates against large variations due to radial-velocity errors. Thus, small shifts in a spectrum due to a poor radial-velocity determination will not strongly influence our estimates of the stellar parameters.

If none of the above methods yields an acceptable estimate of radial velocity, or if the reported velocity is apparently spurious (greater than 1000 km s⁻¹ or less than -1000 km s⁻¹), we simply ignore the spectrum of the star in our subsequent analysis, and set the radial-velocity flag to “NORV.”

2.2. Checks on Radial Velocities—Zero Points and Scatter

In order to check on the accuracy of the radial velocities adopted by the SSPP, we compare them with over 150 high-resolution spectra of SDSS-I/SEGUE stars that have been obtained in order to calibrate and validate the stellar atmospheric parameters. Table 2 summarizes the available high-resolution data. We plan to continue enlarging this sample of validation/calibration stars in the near future.

The high-resolution spectra have been reduced and analyzed independently by two of the present authors (C.A. and T.S.). A detailed description of the analyses can be found in Paper III. During the course of deriving the stellar parameter

Table 1
Parameter Sensitivities to Radial Velocity Errors

Name	RV (km s ⁻¹)	50		100		150		200	
		Method	$\langle \Delta \rangle$	σ	$\langle \Delta \rangle$	σ	$\langle \Delta \rangle$	σ	$\langle \Delta \rangle$
<i>T_{eff}</i>									
Ad	Adop	-0.6	18.8	-22.0	29.5	-48.3	44.4	-83.8	55.0
T1	ki13	21.0	31.3	46.6	64.8	85.4	104.7	113.7	149.0
T2	k24	1.4	8.8	-2.4	16.5	-4.7	30.6	-19.7	53.5
T3	WBG	0.0	12.4	-1.5	6.1	-52.5	70.1	-81.0	106.0
T4	ANNSR	-17.8	72.1	-131.6	100.2	-281.4	153.1	-458.3	232.9
T5	ANNRR	-8.2	15.6	-45.2	39.4	-99.8	67.2	-164.0	95.4
T6	NGS1	7.4	16.9	19.2	35.3	38.7	61.8	55.3	99.1
T7	HA24	-4.6	10.9	-18.9	19.1	-41.1	29.0	-72.0	41.1
T8	HD24	3.8	5.8	2.8	8.1	-0.9	10.1	-5.6	14.8
T9	<i>T_K</i>
T10	<i>T_G</i>
T11	<i>T_I</i>
<i>log g</i>									
Ad	Adop	0.037	0.052	0.071	0.091	0.077	0.135	0.008	0.207
G1	ki13	0.034	0.099	0.066	0.148	0.127	0.224	0.122	0.379
G2	k24	-0.019	0.050	-0.035	0.093	-0.025	0.162	-0.027	0.251
G3	WBG	-0.011	0.039	-0.044	0.198	-0.076	0.413	-0.081	0.620
G4	ANNSR	0.077	0.119	0.151	0.126	-0.236	0.463	-0.317	0.624
G5	ANNRR	0.092	0.068	0.116	0.139	0.046	0.229	-0.103	0.356
G6	NGS1	-0.034	0.054	-0.079	0.145	-0.156	0.293	-0.223	0.464
G7	NGS2	0.012	0.117	-0.001	0.259	-0.009	0.471	-0.131	0.632
G8	CaI1	0.057	0.118	0.143	0.173	0.241	0.249	0.331	0.331
G9	CaI2	-0.042	0.036	-0.116	0.091	-0.233	0.185	-0.385	0.294
G10	MgH	-0.001	0.011	-0.015	0.030	-0.037	0.057	-0.060	0.095
[Fe/H]									
Ad	Adop	-0.019	0.019	-0.096	0.047	-0.203	0.074	-0.353	0.116
M1	ki13	-0.012	0.034	-0.085	0.057	-0.209	0.090	-0.384	0.118
M2	k24	0.002	0.024	-0.057	0.046	-0.192	0.092	-0.404	0.145
M3	WBG	-0.046	0.057	-0.122	0.147	-0.256	0.411	-0.734	0.559
M4	ANNSR	-0.082	0.090	-0.171	0.161	-0.251	0.488	-0.526	0.524
M5	ANNRR	-0.027	0.027	-0.163	0.095	-0.364	0.196	-0.574	0.319
M6	NGS1	-0.008	0.021	-0.056	0.038	-0.157	0.061	-0.292	0.083
M7	NGS2	-0.044	0.033	-0.113	0.074	-0.261	0.136	-0.414	0.219
M8	CaKII1	0.010	0.054	0.029	0.082	0.023	0.144	-0.007	0.238
M9	CaKII2	0.000	0.000	0.014	0.034	0.000	0.095	0.003	0.051
M10	CaKII3	0.001	0.020	0.001	0.032	0.002	0.029	0.006	0.040
M11	ACF	0.005	0.013	0.012	0.021	0.021	0.025	0.030	0.026
M12	CaIIT	-0.000	0.000	0.013	0.071	0.022	0.088	0.062	0.120

Notes. See Section 4 for descriptions of each method. $\langle \Delta \rangle$ is the average of the differences between parameters obtained with, and without, the velocity shift; σ is the standard deviation of the differences. The T9, T10, and T11 estimates do not change with velocity errors because they are computed from the $g - r$ color.

Table 2
Summary of High-Resolution Spectroscopy for SDSS and SEGUE Stars

Telescope	Instrument	Resolving Power	Wavelength Coverage (Å)	Number of Stars
Keck-I	Hires	45000	3800–10000	11
Keck-II	ESI	6000	3800–10000	25
HET	HRS	15000	4400–8000	110
Subaru	HDS	45000	3000–8000	9

estimates from the high-resolution spectra, the radial velocities of the stars are first measured. Note that C.A. considered only the HET spectra, while T.S. considered all available spectra. Thus, only the HET stars have radial velocities obtained by both analysts; for these stars we take an average of their independent determinations, which typically differ by no more than

1–2 km s⁻¹. A more detailed discussion is presented in Paper III.

In this paper we focus on the systematic errors of the adopted radial velocities. After rejecting problematic (e.g., S/N < 20/1) high-resolution spectra, or stars that appear to be spectroscopic binaries at high spectral resolution), 125 stars remain to compare with the adopted radial-velocity results from the SSPP. Figure 1 shows the results of these comparisons. A consistent offset of -6.13 km s⁻¹ (with a standard deviation of 4.71 km s⁻¹) is computed from a Gaussian fit to the residuals; this offset appears constant over the color range $0.1 \leq g - r \leq 0.9$. An additional comparison with the radial-velocity distribution of selected member stars in the Galactic globular and open clusters reveals similar offsets (-8.68 km s⁻¹ for M 15, -7.03 km s⁻¹ for M 13, -8.26 km s⁻¹ for NGC 2420, and -7.47 km s⁻¹ for M 67; see Paper II for the membership selection criteria). The

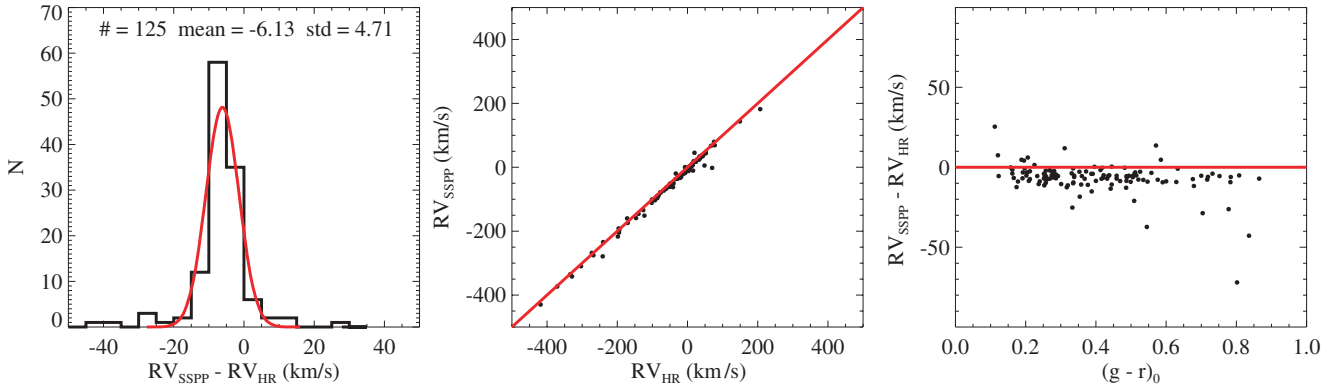


Figure 1. Comparison plots of the radial velocity adopted by the SSPP with that measured by high-resolution analyses (HR). An offset of -6.13 km s^{-1} , with $\sigma = 4.71 \text{ km s}^{-1}$, is noted from the Gaussian fit to the residuals. This offset appears constant with $g - r$, as shown in the right-hand panel.

origin of this velocity offset is as yet unclear; it may stem from the use of different algorithms in the fits to arc and sky lines (Adelman-McCarthy et al. 2008). It should be noted that an offset of $+7.3 \text{ km s}^{-1}$ is added to all DR-6 (Adelman-McCarthy et al. 2008) stellar radial velocities. This offset was computed by averaging the offsets of -6.8 km s^{-1} (M 15), -8.6 km s^{-1} (M 13), and a -6.6 km s^{-1} offset for individual field stars, all obtained from preliminary results of an analysis of the clusters and the high-resolution spectroscopic analysis of SDSS-I/SEGUE stars that were carried out prior to DR-6 (Adelman-McCarthy et al. 2008). In Paper III, this offset is taken into account in the comparison of the radial-velocity determinations. From the new high-resolution spectroscopic analysis of SDSS-I/SEGUE stars (Paper III) and the analysis of member stars of the clusters (Paper II), an average offset is -7.51 km s^{-1} . Therefore, in future data releases (e.g., DR-7), this very minor difference will likely be reflected in all adopted stellar radial velocities. However, in order to account for its presence and to be consistent with the DR-6 database, we apply an empirical $+7.3 \text{ km s}^{-1}$ shift to each adopted radial velocity obtained by the SSPP. After application of this velocity shift, the zero-point uncertainties in the corrected radial velocities determined by the SSPP (and the SDSS spectroscopic reduction pipeline it depends on) should be close to zero, with a random scatter on the order of 5 km s^{-1} or less. Note that the scatter in the determination of radial velocities, based on the average displacements of the “quality assurance” stars with multiple measurements varies from 5.0 km s^{-1} to 9.0 km s^{-1} , depending on spectral type, and exhibits a scatter of 2 km s^{-1} between observations obtained with the “faint” and “bright” spectroscopic plug plates (Adelman-McCarthy et al. 2008).

3. CALCULATION OF LINE INDICES

The initial step in calculation of line indices for SDSS spectra is to transform the wavelength scale of the original SDSS spectrum over to an air-based (rather than vacuum-based) wavelength scale, and to linearly rebin the spectrum to 1 \AA bins in the blue ($3800\text{--}6000 \text{ \AA}$), and 1.5 \AA bins in the red ($6000\text{--}9000 \text{ \AA}$). This slightly larger bin size is due to the degradation of the resolution in the red regions of the spectra. Then, based on the adopted radial velocity described above, the wavelength scale is shifted to a zero-velocity rest frame.

The SSPP measures the line indices of 82 atomic and molecular lines. Line-index calculations are performed in two modes: one uses a global continuum fit over the entire wavelength range ($3850\text{--}9000 \text{ \AA}$), while the other obtains local continuum

estimates around the line bands of interest. The choice of mode used depends on the line depth and width of the feature under consideration. Local continua are employed for the determinations of stellar atmospheric parameters based on techniques that depend on individual line indices. Other techniques, such as the neural network, spectral matching, and autocorrelation methods, require wider wavelength ranges to be considered; for these the global continuum (or their own internal continuum routine) is used. We make use of the errors in the fluxes reported by the SDSS spectroscopic reduction pipeline to measure the uncertainty in the line indices. Details of the procedures used to obtain the continuum fits and line index measures (and their errors) are discussed below.

3.1. Continuum Fit Techniques

3.1.1. Global Continuum Fit

Determination of the appropriate continuum for a given spectrum is a delicate task, even more so when it must be automated, and is obtained for stars with wide ranges of effective temperatures, as is the case for the present application.

In order to obtain a global continuum fit, the SSPP first divides the wavelength range into two pieces: blue ($3850\text{--}5800 \text{ \AA}$) and red ($5800\text{--}9000 \text{ \AA}$). After removing the strong Balmer lines present in most of the spectra, the blue side is iteratively fitted to a ninth-order polynomial, rejecting points that are more than 3σ below the fitted function. The same procedure is applied to the red side, but using a fourth-order polynomial. Then, the two fitted pseudocontinua are spliced together, and the joined continuum is again fitted to a ninth-order polynomial. This is the final global pseudocontinuum used to calculate line indices.

The reason for dividing a spectrum into two regions is to avoid the continuum being placed at too high of a level around the Ca II triplet, due to the poor sky-line subtraction in this region in some cases. Fitting the entire range of a spectrum requires a high-order polynomial. As a result, the continuum on the red side of a spectrum will be artificially boosted due to the presence of poorly subtracted sky lines or noise spikes, if any. Use of a lower-order polynomial fit to the red side avoids this potential problem.

The upper panel of Figure 2 shows an example of a fitted global continuum for a metal-poor giant, obtained by the application of the procedure described above. The atmospheric parameters determined by the SSPP are also listed on the plot. The bottom panel is the normalized spectrum, obtained by the division of the spectrum by the global continuum fit. Strong lines that play important roles in estimating the

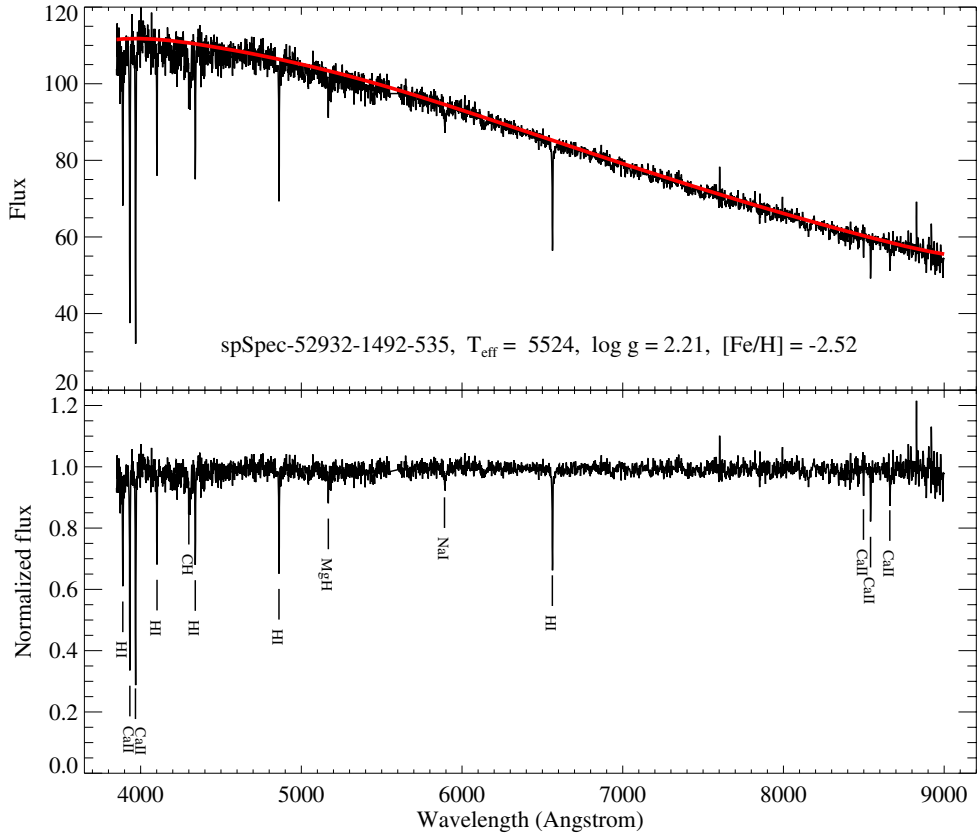


Figure 2. Example of a fitted global continuum for a metal-poor star. The derived parameters from the SSPP for this star are shown in the upper panel. The red line in the upper panel is the fitted continuum over the 3850–9000 Å wavelength range; the black line is the observed spectrum. The bottom panel shows the normalized flux, with strong metal and Balmer features labeled.

atmospheric parameters are labeled. It can be seen that a reasonable continuum estimate is obtained even in the region of the Ca II triplet, where residuals from poor sky subtraction can sometimes be problematic.

3.1.2. Local Continuum Fit

To compute a local continuum over the line band of interest, we first calculate a 5σ -clipped average of the observed fluxes over the (blue and red) sidebands corresponding to each feature, as listed in Table 3. Using these two points, a linear interpolation is carried out over the region between the end point of the blue sideband and the starting point of the red sideband. This linearly interpolated flux is then connected piecewise with the fluxes of the red and blue sidebands, and a robust line fit is performed over the entire region of the blue sideband + line band + red sideband to derive the final local continuum estimate.

3.2. Measurement of Line Indices

Line indices (or equivalent widths) are calculated by integrating a continuum-normalized flux over the specified wavelength regions of each line band. Two different measurements of line indices, obtained from the two different continuum methods described above, are reported, even though the line-index-based methods for stellar parameter estimates only make use of the local-continuum-based indices. In order to avoid spurious values for the derived indices, if a given index measurement is greater than 100 Å, or is negative, we set the reported value to −9.999. No parameter estimates based on that particular line index are used.

Table 3 lists the complete set of line indices made use of by the SSPP. Note that, unlike the case for most of the features in this Table, the line indices listed in rows 74 (TiO_1), 75 (TiO_2), 76 (TiO_3), 77 (TiO_4), 78 (TiO_5), 79 (CaH_1), 80 (CaH_2), 81 (CaH_3), 82 (CaOH), and 83 ($\text{H}\alpha$) are calculated following the prescription given by the “Hammer” program (Covey et al. 2007). The line index for Ca I at 4227 Å, and the Mg I b and Mg H features around 5170 Å, are computed following Morrison et al. (2003), so that they might be used to estimate $\log g$, as described in Section 4.8.

We follow the Cayrel (1988) procedure to compute an error for each line index measurement. The uncertainty (EW_{error}) in the index or measured equivalent width is

$$\text{EW}_{\text{error}} = \frac{1.6 \times (\text{resolution} \times \text{pixel size})^{1/2}}{\text{S/N}}, \quad (1)$$

where S/N is the signal-to-noise ratio in the local region of the spectrum, the *resolution* is taken to be ~ 2.5 Å, and the *pixel size* is set to 1 Å for the blue region (3800–6000 Å), and 1.5 Å for the red region (6000–9000 Å), respectively. The noise spectrum provided by the SDSS spectroscopic reduction procedure is used to compute the local S/N.

4. METHODOLOGY

The SSPP employs a number of methods for estimation of effective temperature, surface gravity, and metallicity, based on SDSS spectroscopy and photometry. In this section the methods used by the SSPP are summarized. Since many of the methods implemented in the SSPP are already described by

Table 3
Line Band and Sideband Widths and Format of the Output from the SSPP

Column	Format	Description	Central (Å)	Width (Å)	Red (Å)	Width (Å)	Blue (Å)	Width (Å)
1	A22	spSpec name
2	F8.3	H8 (3)	3889.0	3.0	3912.0	8.0	3866.0	8.0
3	F8.3	H8 (12)	3889.1	12.0	4010.0	20.0	3862.0	20.0
4	F8.3	H8 (24)	3889.1	24.0	4010.0	20.0	3862.0	20.0
5	F8.3	H8 (48)	3889.1	48.0	4010.0	20.0	3862.0	20.0
6	F8.3	Ca II K12 (12)	3933.7	12.0	4010.0	20.0	3913.0	20.0
7	F8.3	Ca II K18 (18)	3933.7	18.0	4010.0	20.0	3913.0	20.0
8	F8.3	Ca II K6 (6)	3933.7	6.0	4010.0	20.0	3913.0	20.0
9	F8.3	Ca II K30 (30)	3933.6	30.0	4010.0	5.0	3910.0	5.0
10	F8.3	Ca II H & K (75)	3962.0	75.0	4010.0	5.0	3910.0	5.0
11	F8.3	He ε (50)	3970.0	50.0	4010.0	5.0	3910.0	5.0
12	F8.3	Ca II K16 (16)	3933.7	16.0	4018.0	20.0	3913.0	10.0
13	F8.3	Sr II (8)	4077.0	8.0	4090.0	6.0	4070.0	4.0
14	F8.3	He I (12)	4026.2	12.0	4154.0	20.0	4010.0	20.0
15	F8.3	Hδ (12)	4101.8	12.0	4154.0	20.0	4010.0	20.0
16	F8.3	Hδ (24)	4101.8	24.0	4154.0	20.0	4010.0	20.0
17	F8.3	Hδ (48)	4101.8	48.0	4154.0	20.0	4010.0	20.0
18	F8.3	Hδ (64)	4102.0	64.0	4154.0	20.0	4010.0	20.0
19	F8.3	Ca I (4)	4226.0	4.0	4232.0	4.0	4211.0	6.0
20	F8.3	Ca I (12)	4226.7	12.0	4257.0	20.0	4154.0	20.0
21	F8.3	Ca I (24)	4226.7	24.0	4257.0	20.0	4154.0	20.0
22	F8.3	Ca I (6)	4226.7	6.0	4257.0	20.0	4154.0	20.0
23	F8.3	G-band (15)	4305.0	15.0	4367.0	10.0	4257.0	20.0
24	F8.3	Hγ (12)	4340.5	12.0	4425.0	20.0	4257.0	20.0
25	F8.3	Hγ (24)	4340.5	24.0	4425.0	20.0	4257.0	20.0
26	F8.3	Hγ (48)	4340.5	48.0	4425.0	20.0	4257.0	20.0
27	F8.3	Hγ (54)	4340.5	54.0	4425.0	20.0	4257.0	20.0
28	F8.3	He I (12)	4471.7	12.0	4500.0	20.0	4425.0	20.0
29	F8.3	G-blue (26)	4305.0	26.0	4507.0	14.0	4090.0	12.0
30	F8.3	G-whole (28)	4321.0	28.0	4507.0	14.0	4096.0	12.0
31	F8.3	Ba II (6)	4554.0	6.0	4560.0	4.0	4538.0	4.0
32	F8.3	¹² C+ ¹³ C (36)	4737.0	36.0	4770.0	20.0	4423.0	10.0
33	F8.3	¹² C (256)	4618.0	256.0	4780.0	5.0	4460.0	10.0
34	F8.3	Metal-1 (442)	4584.0	442.0	4805.8	5.0	4363.0	5.0
35	F8.3	Hβ (12)	4862.3	12.0	4905.0	20.0	4790.0	20.0
36	F8.3	Hβ (24)	4862.3	24.0	4905.0	20.0	4790.0	20.0
37	F8.3	Hβ (48)	4862.3	48.0	4905.0	20.0	4790.0	20.0
38	F8.3	Hβ (60)	4862.3	60.0	4905.0	20.0	4790.0	20.0
39	F8.3	C₂ (204)	5052.0	204.0	5230.0	20.0	4935.0	10.0
40	F8.3	C₂+Mg I (238)	5069.0	238.0	5230.0	20.0	4935.0	10.0
41	F8.3	MgH+Mg I+C₂ (270)	5085.0	270.0	5230.0	20.0	4935.0	10.0
42	F8.3	MgH+Mg I (44)	5198.0	44.0	5230.0	20.0	4935.0	10.0
43	F8.3	MgH (20)	5210.0	20.0	5230.0	20.0	4935.0	10.0
44	F8.3	Cr I (12)	5206.0	12.0	5239.0	8.0	5197.5	5.0
45	F8.3	Mg I + Fe II (20)	5175.0	20.0	5240.0	10.0	4915.0	10.0
46	F8.3	Mg I (2)	5183.0	2.0	5240.0	10.0	4915.0	10.0
47	F8.3	Mg I (12)	5170.5	12.0	5285.0	20.0	5110.0	20.0
48	F8.3	Mg I (24)	5176.5	24.0	5285.0	20.0	5110.0	20.0
49	F8.3	Mg I (12)	5183.5	12.0	5285.0	20.0	5110.0	20.0
50	F8.3	Na I (20)	5890.0	20.0	5918.0	6.0	5865.0	10.0
51	F8.3	Na I (12)	5892.9	12.0	5970.0	20.0	5852.0	20.0
52	F8.3	Na I (24)	5892.9	24.0	5970.0	20.0	5852.0	20.0
53	F8.3	Hα (12)	6562.8	12.0	6725.0	50.0	6425.0	50.0
54	F8.3	Hα (24)	6562.8	24.0	6725.0	50.0	6425.0	50.0
55	F8.3	Hα (48)	6562.8	48.0	6725.0	50.0	6425.0	50.0
56	F8.3	Hα (70)	6562.8	70.0	6725.0	50.0	6425.0	50.0
57	F8.3	CaH (505)	6788.0	505.0	7434.0	10.0	6532.0	5.0
58	F8.3	TiO (333)	7209.0	333.0	7434.0	10.0	6532.0	5.0
59	F8.3	CN (26)	6890.0	26.0	7795.0	10.0	6870.0	10.0
60	F8.3	O I tri (30)	7775.0	30.0	7805.0	10.0	7728.0	10.0
61	F8.3	K I (34)	7687.0	34.0	8080.0	10.0	7510.0	10.0
62	F8.3	K I (95)	7688.0	95.0	8132.0	5.0	7492.0	5.0
63	F8.3	Na I (15)	8187.5	15.0	8190.0	55.0	8150.0	10.0

Table 3
(Continued)

Column	Format	Description	Central (Å)	Width (Å)	Red (Å)	Width (Å)	Blue (Å)	Width (Å)
64	F8.3	Na I-red (33)	8190.2	33.0	8248.6	5.0	8140.0	5.0
65	F8.3	Ca II tri (26)	8498.0	26.0	8520.0	10.0	8467.5	25.0
66	F8.3	Paschen (13)	8467.5	13.0	8570.0	14.0	8457.0	10.0
67	F8.3	Ca II tri (29)	8498.5	29.0	8570.0	14.0	8479.0	10.0
68	F8.3	Ca II tri (40)	8542.0	40.0	8570.0	14.0	8479.0	10.0
69	F8.3	Ca II tri (16)	8542.0	16.0	8600.0	60.0	8520.0	20.0
70	F8.3	Paschen (42)	8598.0	42.0	8630.5	23.0	8570.0	14.0
71	F8.3	Ca II tri (16)	8662.1	16.0	8694.0	12.0	8600.0	60.0
72	F8.3	Ca II tri (40)	8662.0	40.0	8712.5	25.0	8630.5	23.0
73	F8.3	Paschen (42)	8751.0	42.0	8784.0	16.0	8712.5	25.0
74	F7.3	TiO ₁ (5)	6720.5	5.0	6720.5	5.0	6705.5	5.0
75	F7.3	TiO ₂ (5)	7059.5	5.0	7059.5	5.0	7044.5	5.0
76	F7.3	TiO ₃ (5)	7094.5	5.0	7094.5	5.0	7081.5	5.0
77	F7.3	TiO ₄ (5)	7132.5	5.0	7132.5	5.0	7117.5	5.0
78	F7.3	TiO ₅ (9)	7130.5	9.0	7130.5	9.0	7044.0	4.0
79	F7.3	CaH ₁ (10)	6385.0	10.0	6415.0	10.0	6350.0	10.0
80	F7.3	CaH ₂ (32)	6830.0	32.0	6830.0	32.0	7044.0	4.0
81	F7.3	CaH ₃ (30)	6975.0	30.0	6975.0	30.0	7044.0	4.0
82	F7.3	CaOH (10)	6235.0	10.0	6235.0	10.0	6349.5	9.0
83	F7.3	H α (6)	6563.0	6.0	6563.0	6.0	6550.0	10.0

Note. The number in parentheses is the line band width in Å.

Table 4

Comparison of Parameters from NGS1 and NGS2 grids with ELODIE and MILES Libraries and High-Resolution Values

Grid	Library	S/N	N	T _{eff}		log g		[Fe/H]	
				$\langle \Delta \rangle$	σ	$\langle \Delta \rangle$	σ	$\langle \Delta \rangle$	σ
				(K)	(K)	(dex)	(dex)	(dex)	(dex)
NGS1									
ELODIE	Full	620	+12	74	+0.11	0.24	-0.22	0.11	
ELODIE	50/1	617	+10	87	+0.09	0.25	-0.23	0.12	
ELODIE	25/1	617	+13	103	+0.09	0.28	-0.21	0.14	
ELODIE	12.5/1	601	+15	175	+0.13	0.37	-0.09	0.19	
ELODIE	6.25/1	541	+36	269	+0.25	0.50	+0.23	0.29	
MILES	Full	403	+64	120	+0.10	0.31	-0.24	0.13	
HR	Full	81	+85	164	+0.13	0.30	-0.24	0.16	
NGS2									
ELODIE	Full	615	+0.15	0.26	-0.22	0.13	
MILES	Full	385	+0.16	0.29	-0.24	0.15	
HR	Full	81	+0.17	0.29	-0.25	0.13	

Note. HR comes from the results of HA1 which is used in Paper III to determine empirical errors of the SSPP parameters.

previously published papers, we will address those techniques briefly, and refer the reader to individual papers for detailed descriptions. The methods that are introduced here for the first time are explained in more detail. Note that some approaches derive all three atmospheric parameters simultaneously, while others are specific to an individual parameter. A given method is usually optimal over specific ranges of color, $g - r$, and S/N. Table 5 lists the ranges we have adopted in these observables for the SSPP. Details regarding the choice of the S/N cuts are presented in Section 6.

4.1. Spectral Fitting with the k24 and ki13 Grids

These two methods are based on the identification of parameters for a model atmosphere that best matches the observed fluxes in a selected wavelength interval, as described in detail by

Allende Prieto et al. (2006). Classical LTE line-blanketed model atmospheres are used to compute a discrete grid of fluxes; interpolation allows subgrid resolution. The search is performed using the Nelder–Mead algorithm (Nelder & Mead 1965).

The k24 grid described by Allende Prieto et al. (2006) is used by the SSPP. It includes a predicted broadband color index $g - r$, as well as normalized spectral fluxes in the region 4400–5500 Å, at a resolving power of $R = 1000$. R. L. Kurucz's (1993, private communication) model atmospheres and simplified continuum opacities are used to calculate synthetic spectra. The synthetic broadband photometry was derived from the spectral energy distributions provided by Kurucz (1993), using the passbands for point sources determined by Strauss & Gunn (2001) and an assumed (average) air mass of 1.3.

In addition to the k24 grid, a second grid, referred to as ki13, is implemented in the SSPP. This second grid covers the same spectral window as the k24, but no photometry is considered. The use of only the normalized spectra de-couples the results based on this grid from reddening and photometric errors, although valuable information, mainly on the effective temperature, is sacrificed.

There are several other differences between k24 and ki13 grids. The new grid (ki13) includes molecular line opacities, with the most relevant molecules in the range of interest being the CH G-band near 4300 Å, as well as the MgH band. In addition, the ki13 grid takes advantage of a novel concept that allows for a significant increase in the speed of the calculation of model fluxes. The relevant opacities are not calculated for all depths in all models, but instead are obtained on a temperature and density grid, and later interpolated to the exact points in any given model atmosphere (Koesterke et al. 2008). The opacity grid includes four points per decade in density and steps of 125 K in temperature. With these choices, linear interpolation leads to errors in the normalized fluxes smaller than 1%.

Allende Prieto et al. (2006) made use of several libraries of observed spectra and atmospheric parameters to study systematic and random errors obtained from the k24 analysis. Even

Table 5
Valid Ranges of $g - r$ and S/N for Individual Methods in the SSPP

T_{eff}			$\log g$			[Fe/H]			S/N	Reference
Name	Method	$g - r$	Name	Method	$g - r$	Name	Method	$g - r$		
T1	ki13	0.0–0.8	G1	ki13	0.0–0.8	M1	ki13	0.0–0.8	≥ 15	Section 4.1
T2	k24	0.0–0.8	G2	k24	0.0–0.8	M2	k24	0.0–0.8	≥ 15	Allende Prieto et al. (2006)
T3	WBG	−0.3–0.8	G3	WBG	−0.3–0.8	M3	WBG	−0.3–0.8	≥ 10	Wilhelm et al. (1999)
T4	ANNSR	−0.3–0.8	G4	ANNSR	−0.3–0.8	M4	ANNSR	−0.3–0.8	≥ 20	Section 4.3
T5	ANNRR	−0.3–1.2	G5	ANNRR	−0.3–1.2	M5	ANNRR	−0.3–1.2	≥ 10	Re Fiorentin et al. (2007)
T6	NGS1	−0.3–1.3	G6	NGS1	−0.3–1.3	M6	NGS1	−0.3–1.3	≥ 15	Section 4.4
...	G7	NGS2	0.0–1.3	M7	NGS2	0.0–1.3	≥ 20	Section 4.4
...	G8	CaII1	−0.3–0.8	M8	CaIIK1	−0.3–0.8	≥ 10	Section 4.5
...	0.4–0.9	M9	CaIIK2	0.1–0.8	≥ 10	Beers et al. (1999)
...	0.4–0.9	M10	CaIIK3	0.1–0.8	≥ 10	Section 4.6
...	M11	ACF	0.1–0.9	≥ 15	Beers et al. (1999)
...	M12	CaIIT	0.1–0.7	≥ 20	Cenarro et al. (2001a, 2001b)
...	G9	CaI2	0.4–0.9	≥ 10	Morrison et al. (2003)
...	G10	MgH	0.4–0.9	≥ 10	Morrison et al. (2003)
T7	HA24	0.0–0.8	≥ 10	Section 5.1
T8	HD24	0.0–0.6	≥ 10	Section 5.1
T9	T_K	−0.3–1.3	N/A	Section 5.1
T10	T_G	−0.3–1.3	N/A	Section 5.1
T11	T_I	−0.3–1.3	N/A	Ivezic et al. 2008

Notes. HA24 and HD24 are the temperature estimates from the H α and H δ line indices in 24 Å widths, respectively. The temperature estimated from Kurucz models is referred to as T_K ; T_G is for the Girardi et al. (2004) isochrones. T_I is the temperature determined from Equation (8). The S/N cut is not applied to these temperature estimates because they are computed based on the $g - r$ color. The ki13, k24, NGS1, and NGS2 are grid-matching-based methods. WBG is the method from Wilhelm et al. (1999). ANNSR and ANNRR are the neural network approaches. CaIIK1 and CaI1 are determined from the 3850–4250 Å region. CaI2 and MgH are methods based on Morrison et al. (2003). CaIIK2 and CaIIK3 are the [Fe/H] estimates based on the Ca II K line. ACF is the autocorrelation function method, and CaIIT is based on the Ca II triplet line index. S/N is the average S/N per pixel over the spectral region 4000 Å to 8000 Å. See Section 4 for detailed descriptions of individual methods and Section 6 for the S/N cuts. The nominal (“n”) flag is raised for parameters which are based on spectra that satisfy at least some of the criteria listed above. However, for spectra with $5/1 \leq S/N < 10/1$, which would usually be rejected by strict application of the cuts above, the parameters are reported with the “P” flag raised. No parameters are reported for spectra with $S/N < 5/1$, and the “N” flag is raised.

at infinite S/Ns, random errors appear significantly larger than systematic errors, and amount to 3% in T_{eff} , 0.3 dex in $\log g$, and 0.2 dex in [Fe/H]. This is most likely the result of using oversimplified model fluxes with a solar-scaled abundance pattern (including an enhancement of the α elements at low iron abundance), which is too limited to account for the chemical spread in real stars. The new ki13 grid offers a significant improvement in random errors, which at high S/Ns amounts to 2% in T_{eff} , 0.2 dex in $\log g$, and 0.1 dex in [Fe/H], but a less robust behavior (due to the lack of color information) at low S/Ns. Small systematic offsets in ki13 detected from the analysis of the spectra in the ELODIE library (Prugniel & Soubiran 2001) are corrected using linear transformations.

As discussed in Allende Prieto et al. (2006), the k24 approach performs best in the color range of roughly $0.0 \leq g - r \leq 0.8$; this range is also applied to the ki13 grid. When it is run, the SSPP restricts the adopted parameters from these methods to fall in this color range. The SSPP refers to the T_{eff} , $\log g$, and [Fe/H] estimated with the ki13 grid as T1, G1, and M1, respectively, while the parameters estimated from the k24 grid are referred to as T2, G2, and M2, respectively.

4.2. Parameters Obtained from the Wilhelm et al. (1999) Procedures: WBG

This method, which is referred to as WBG in this paper, is based on the routines described by Wilhelm et al. (1999), to which we refer the interested reader. Extensions of this method, as used in the SSPP, are described below.

The procedures implemented in the SSPP are optimized for two separate temperature ranges, one for the warmer stars ($g - r \leq 0.25$) and the other for the cooler stars, with redder colors than this limit. The stellar parameter determinations make use of comparisons to theoretical ugr colors and line parameters from synthetic spectra, both generated from ATLAS9 model atmospheres (Kurucz 1993). The synthetic spectra used in these procedures were generated using the spectral synthesis routine SPECTRUM (Gray & Corbally 1994).

For the hotter stars, the Balmer lines of the observed normalized spectra are fitted with a Voigt profile to determine the Balmer-line equivalent widths and the $D_{0.2}$ (the line width at 20% below the local pseudocontinuum level) widths for H δ , H γ , and H β . The combination of Balmer-line equivalent widths, $D_{0.2}$, and $u - g$ and $g - r$ colors are used to establish initial T_{eff} and $\log g$ estimates, computed from functional trends in the theoretical model parameters. For stars cooler than $T_{\text{eff}} \sim 8000$ K, the surface gravity is mainly determined by the $u - g$ color. For hotter stars the surface gravity is primarily determined by the $D_{0.2}$ parameter. A metallicity estimate is determined through the use of a combination of the equivalent width of the Ca II K line and a comparison to synthetic spectral regions that contain other (much weaker) metallic lines. Once an initial abundance is established, the procedure is iterated to convergence in all three stellar parameters.

For the cooler stars, only the $g - r$ color is used to establish an initial estimate of T_{eff} . For these stars, $\log g$ is determined from the $u - g$ color for stars as cool as $T_{\text{eff}} = 5750$ K. For stars cooler than this limit, the strength of MgH is compared with

synthetic spectra of similar T_{eff} and [Fe/H] through the use of a band-strength indicator. The metal abundance is determined by the combination of the Ca II K line strength and a minimum χ^2 comparison to metallic-line regions in the spectra. The procedure is then iterated to convergence.

For stars with $S/N \geq 10/1$, the derived errors for the WBG approach are on the order of $\sigma(T_{\text{eff}}) = 225$ K, $\sigma(\log g) = 0.25$ dex, and $\sigma([\text{Fe}/\text{H}]) = 0.3$ dex. The color range of $g - r$ over which this approach is used for the SSPP is $-0.3 \leq g - r \leq 0.8$. The effective temperature, surface gravity, and [Fe/H] estimated from this technique are referred to as T3, G3, and M3, respectively.

4.3. The Neural Network Approaches: ANNRR and ANNSR

The SSPP implements flexible methods of regression that provide a global nonlinear mapping between a set of inputs (the stellar spectrum \mathbf{x}_i) and a set of outputs (the stellar atmospheric parameters, $\mathbf{s} = \{T_{\text{eff}}, \log g, [\text{Fe}/\text{H}]\}$). These methods have been described in detail by Re Fiorentin et al. (2007), to which we refer the interested reader.

For the present application, it should be noted that we have chosen not to include the input photometry, although this could certainly be added if desired. Moreover, thanks to improved stellar models and data calibrations the models have been further developed in order to investigate the impact of noise and to extend the application of neural networks for low signal-to-noise spectra (P. Re Fiorentin et al. 2008, in preparation).

The procedures implemented in the SSPP use an initial Principal Component Analysis compression of the data, and are based on two different approaches—training the model on real (RR, e.g., SDSS spectra) or synthetic (SR) spectra to obtain atmospheric-parameter estimates for the observed spectra. The method for training the model on the SDSS/SEGUE spectra is called ANNRR, while that for the synthetic spectra is referred to as ANNSR.

4.3.1. The ANNRR Approach

We build the models based on a set of 61,069 selected stars from the current SEGUE plug plates, in directions of low reddening, for which atmospheric parameters were estimated by a preliminary version of the SSPP.

The RR regression model (ANNRR) adopts a sample that is randomly split into two equal-sized sets, one for training and the other for evaluation. Although not optimal, as one would ideally like to use a completely independent basis set for the training, this approach automates and—more importantly—generalizes the basis parameterizer. Indeed, the basis parameterizer may even comprise multiple algorithms, perhaps operating over different parameter ranges or used in a voting system to estimate atmospheric parameters. This is true in the present case, where the basis parameterizer comes from a preliminary version of the SSPP.

The two upper sets of panels in Figure 3 compare the stellar parameters obtained from the ANNRR approach with those from an earlier version of the SSPP adopted parameters, based on an evaluation set of some 30,000 SEGUE spectra. Overall we see good consistency, especially for stars with $T_{\text{eff}} < 8000$ K ($\log T_{\text{eff}} = 3.90$). Above this effective temperature our models slightly underestimate $\log T_{\text{eff}}$ relative to the SSPP adopted values. Most regression models such as ours are designed to interpolate, rather than extrapolate. Extrapolation of the model to estimate atmospheric parameters that are not spanned by the

training set is relatively unconstrained. Furthermore, the accuracy of the RR model is limited by the accuracy of the target atmospheric parameters used in training, as well as their consistency across the parameter space. In this case, the SSPP estimates are combinations from several estimation models, each of which operates only over a limited parameter range. Thus, the transition we see above 8000 K may indicate a temperature region where one of the SSPP submodels dominates the SSPP estimates; such cases are not well generalized by our model. From this comparison, we find that the accuracies of our predictions (mean absolute errors) for each parameter are $\sigma(T_{\text{eff}}) = 60$ K, $\sigma(\log g) = 0.11$ dex, and $\sigma([\text{Fe}/\text{H}]) = 0.07$ dex, which are very low. This is partly due to the fact that the ANNRR method makes use of exactly the same type of data used in the training and application phases, thus eliminating the issue of discrepancies in the flux calibration or cosmic variance of the two samples.

4.3.2. The ANNSR Approach

Recently, an adequate noise model for SDSS spectra has been developed by one of the authors (C.R., see Section 6 for details). The SR regression model (ANNSR) adopts a sample of these noise-added synthetic spectra as the training set. This approach thus directly models the mapping between synthetic spectra and the atmospheric parameters, independent of any intermediate estimates. The ANNSR method is optimized to be able to deal separately with low-S/N real spectra ($S/N < 35/1$, 22,196 stars) and high-S/N real spectra ($S/N > 35/1$, 38,873 stars).

The two lower sets of panels in Figure 3 compare the atmospheric-parameter estimates from the ANNSR with those from the SSPP for the 61,069 stars in the evaluation set. While the overall consistency between the two models is reasonably good, we note discrepancies at the extreme parameter values, in particular for T_{eff} and $\log g$.

Despite the fact that determinations of gravity and metallicity for low-S/N spectra are underestimated, as measured by their mean accuracies with respect to the SSPP predictions, we can obtain estimates of T_{eff} with residuals of $\sim 125/129$ K, $\log g$ with residuals of $0.21/0.28$ dex, and [Fe/H] with residuals of $0.14/0.23$ dex for the high-/low-S/N regimes, respectively. The neural network approaches included in the SSPP are currently limited to $S/N \geq 10/1$.

The advantage of the ANNSR approach is that it is trained directly on synthetic spectra, dispensing with the need for a basis parameterizer. A very important aspect of this method is to process the synthetic and real data to appear as similar as possible; noise acts as a regularizer in the training phase. Inaccurate synthetic spectra (e.g., poor models or a poor flux calibration) degrade performance and/or give rise to systematic errors. However, there are inevitably problems with spectral mismatches, in the sense that the synthetic spectra do not reproduce all of the complexities of the spectra of real stars. The absence of some molecular species in the line lists for the synthetic spectra may also be contributing to this problem, especially for cooler stars where they are expected to become more important.

Prior experience with the behavior of the neural network approach on the SDSS-I/SEGUE data indicated that the ANNRR performs well over a color range $-0.3 \leq g - r \leq 1.2$, so we restrict its application for the SSPP to this interval. The color range is restricted to $-0.3 \leq g - r \leq 0.8$ for the ANNSR estimates. The T_{eff} , $\log g$, and [Fe/H] obtained from the ANNSR approach are referred to as T4, G4, and M4, respectively; for

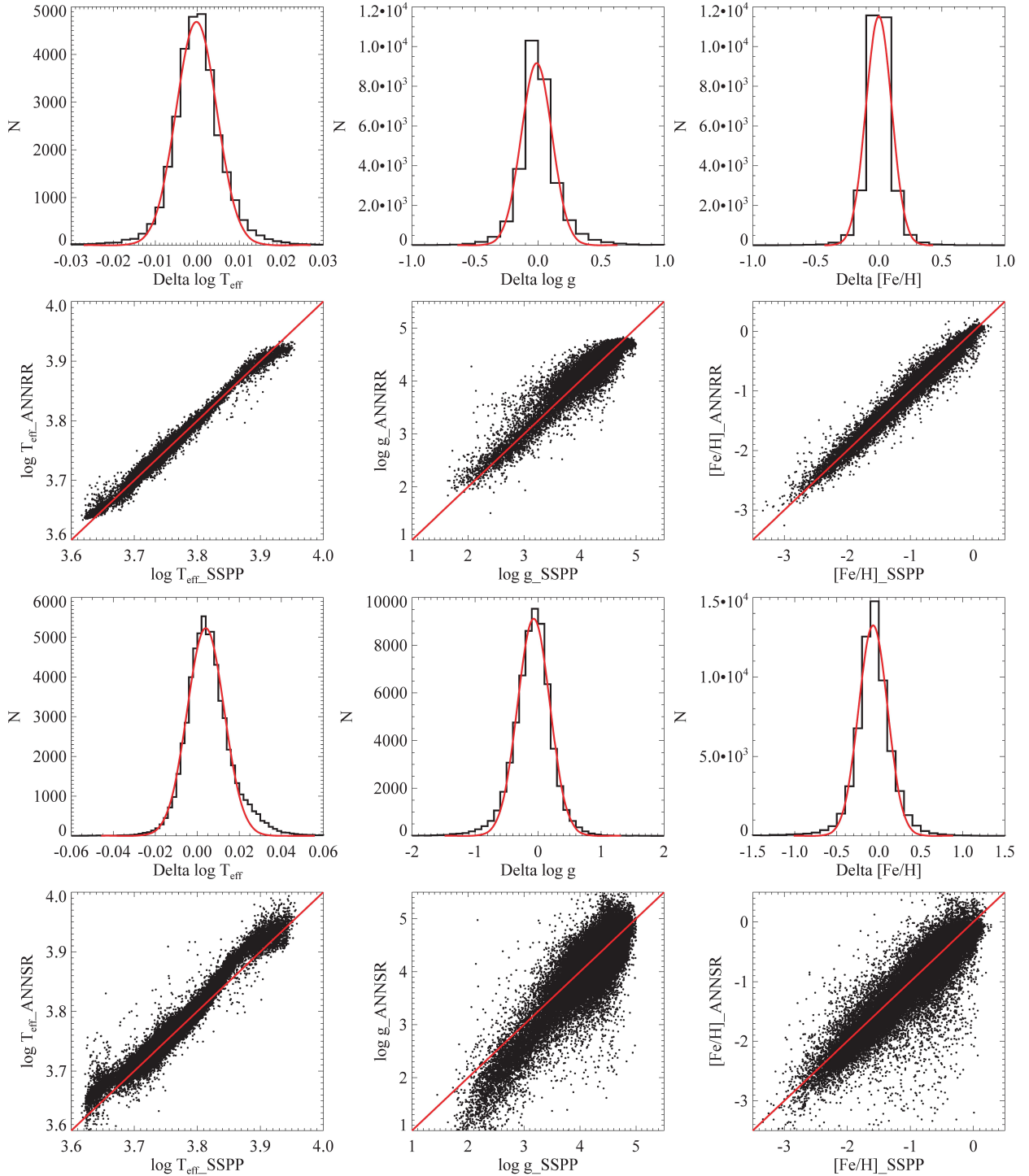


Figure 3. Atmospheric-parameter estimation with ANNRR (two upper sets of panels) and ANNSR (two lower sets of panels). We compare $\log T_{\text{eff}}$, $\log g$, and $[\text{Fe}/\text{H}]$ estimates from ANNRR and ANNSR with those from the SSPP. There are 30,000 stars compared for the ANNRR approach and 61,069 stars for ANNSR. Perfect correlation is shown with the solid red lines. The histograms of the discrepancies between the ANNRR and ANNSR approaches and the SSPP are shown in the first and third sets of panels, with a Gaussian fit shown as a red curve.

the ANNRR approach, they are referred to as T5, G5, and M5, respectively.

4.4. The χ^2 Minimization Technique Using the NGS1 and NGS2 Grids

4.4.1. Grids of Synthetic Spectra

We have made use of Kurucz's NEWODF models (Castelli & Kurucz 2003), which employ solar relative abundances

from Grevesse & Sauval (1998), to generate two sets of grids of synthetic spectra. The model atmospheres assume plane-parallel line-blanketed model structures in one-dimensional local thermodynamical equilibrium (LTE), and an enhancement of alpha-element abundances by +0.4 dex for stars with $[\text{Fe}/\text{H}] \leq -1.0$ and +0.3, +0.2, and +0.1 for $[\text{Fe}/\text{H}] = -0.75$, -0.5, and -0.25, respectively. These new models include H_2O opacities, an improved set of TiO lines, and no convective overshoot (Castelli et al. 1997).

For production of the synthetic spectra we employed the `turbospectrum` synthesis code (Alvares & Plez 1998), with solar abundances from Asplund et al. (2005), which use the treatment of line broadening described by Barklem & O’Mara (1998). The sources of atomic lines used by `turbospectrum` mainly come from the VALD database (Kupka et al. 1999). Line lists for the molecular species CH, CN, OH, TiO, and CaH were provided by B. Plez (see Plez & Cohen 2005; B. Plez 2007, private communication), while the lines of NH, MgH, and the C₂ molecules were adopted from the Kurucz line lists.¹³ The grid of the synthetic spectra has a resolution of 0.01 Å or 0.005 Å, and spans from 3500 K $\leq T_{\text{eff}}$ \leq 10,000 K in steps of 250 K, 0.0 $\leq \log g \leq 5.0$ in steps of 0.25 dex, and $-4.0 \leq [\text{Fe}/\text{H}] \leq +0.5$ in steps of 0.25 dex. The wavelength coverage is from 3000 Å to 10,000 Å. The microturbulence was assumed to be 2 km s⁻¹. These synthetic spectra are referred to as the NGS1 grid. After their generation, these synthetic spectra were degraded to $R = 1000$, using a Gaussian convolution algorithm, then sampled into 1.67 Å per pixel for application of the NGS1 grid spectral matching technique described below. There are two reasons for the degradation of the spectra to the lower resolution than that of the SDSS spectra. First, degrading the observed spectrum allows us to obtain higher S/N than the original; more reliable estimates of the parameters can thus be determined. Second, this grid is also used for the application of the SSPP to non-SDSS spectra with lower resolution ($1000 \leq R \leq 2000$; e.g., Beers et al. 2007).

A second grid of model atmospheres was constructed from the Kurucz ATLAS9 models (Castelli & Kurucz 2003), which do not employ alpha-element enhancements for models with $[\text{Fe}/\text{H}] \leq -0.5$. The `turbospectrum` synthesis code was again used to generate the synthetic spectra. The synthetic spectra have a resolution of 0.1 Å, and cover 4000 K $\leq T_{\text{eff}} \leq$ 8000 K in steps of 250 K, 0.0 $\leq \log g \leq 5.0$ in steps of 0.25 dex, and $-3.0 \leq [\text{Fe}/\text{H}] \leq +0.5$ in steps of 0.25 dex. Ranges in $[\alpha/\text{Fe}]$ were introduced for spectral synthesis, over $-0.2 \leq [\alpha/\text{Fe}] \leq +0.8$, in steps of 0.2 dex for each value of T_{eff} , $\log g$, and $[\text{Fe}/\text{H}]$. The spectral range of this grid is 4500 Å–5500 Å. The microturbulence was assumed to be 2 km s⁻¹. These synthetic spectra are referred to as the NGS2 grid. This grid is smoothed to the resolution of the SDSS spectrographs ($R = 2000$); in contrast to the NGS1 grid, this grid is not degraded to a lower resolution. We retain the full resolution of this grid to enable the development of (future) methods for the determination of $[\alpha/\text{Fe}]$ for stars in the range 4000 K $\leq T_{\text{eff}} \leq$ 8000 K (Y. S. Lee et al. 2008, in preparation). Since this is an independent grid, it is also possible to obtain another set of predicted stellar atmospheric parameters for the stars within this temperature range.

4.4.2. Pre-processing Observed Spectra for the χ^2 Minimization Technique

The observed SDSS spectra are processed as described in Section 3 above. The blue region of the spectrum contains most of the information required to constrain the stellar parameters, but for cooler stars, the observed S/N peaks in the red region. As a compromise, and in order to speed up the analysis, we only consider the spectral range 4500–5500 Å. For the NGS2 grid, we sample the spectrum into 1 Å bins; 1.67 Å bins are used for the NGS1 grid, after degrading to $R = 1000$.

¹³ See <http://kurucz.harvard.edu/LINELISTS/LINESMOL/>

The spectrum under consideration is normalized after obtaining a pseudocontinuum over the 4500–5500 Å range. The continuum fit is carried out in a similar fashion to that described in Section 3, but iteratively rejecting the points which lie 1σ below and 4σ above the fitted function, obtained from a eighth-order polynomial. The synthetic spectra used to match with the observed spectra are also normalized in the same fashion over the same wavelength range.

4.4.3. The Parameter Search Technique

Following the above steps, we next carry out a search for the best-fit model parameters, i.e., those that minimize the difference between the observed flux vector, O , and the synthetic flux vector, S , as functions of T_{eff} , $\log g$, and $[\text{Fe}/\text{H}]$, using a reduced χ^2 criterion. That is,

$$\chi^2/\text{DOF} = \sum_{i=1}^{m+1} (O_i - S_i)^2 / \sigma_i^2, \quad (2)$$

where σ_i is the error in flux in the i th pixel and DOF is the number of degrees of freedom.

To reduce the number of model spectra that must be considered in the calculation of the reduced χ^2 values, we first obtain an approximate effective temperature based on a simple approach. This procedure, which we refer to as the Half Power Point (HPP) method (Wisotzki et al. 2000), obtains an estimate of the wavelength at which the total integrated flux over a spectrum is equal to half of the flux obtained over the entire wavelength region (in this case we use 3900–8000 Å). Since the flux distribution for a given stellar spectrum varies strongly with effective temperature, once we have determined the HPP wavelength, we are able to obtain a reasonably accurate estimate of effective temperature (or a broadband color such as $g - r$) by comparing with the HPP wavelengths obtained from a grid of synthetic spectra. The relation between effective temperature and HPP wavelength is established by fitting a polynomial:

$$T_{\text{eff}} = (25.63 - 114.51 \cdot \text{HPP} + 177.17 \cdot \text{HPP}^2 - 93.55 \cdot \text{HPP}^3) \times 10,000 \text{ K}, \quad (3)$$

where $\text{HPP} = \lambda/10,000$.

We initially select synthetic spectra over a broad range around this predicted effective temperature, within ± 1500 K. For example, if the HPP predicted temperature of a star is 5000 K, we consider models between 3500 K and 6500 K. As long as the observed spectrum does not have a grossly incorrect spectrophotometric calibration, the estimated temperature will be well within this range. We then obtain the reduced χ^2 values between the observed and the selected synthetic spectra over a 4500–5500 Å wavelength window.

After trying out several function minimization techniques (e.g., Nelder & Mead 1965), we found that a simple biweight average of several dozen of the lowest reduced χ^2 values is sufficiently fast for computation in the IDL code used in the SSPP, and predicts the stellar parameters with the desired accuracy (≤ 0.30 dex in $[\text{Fe}/\text{H}]$), thanks to the dense grid of the synthetic spectra employed. It also returns a robust estimate of the parameters for lower-S/N (<20/1) spectra.

Note, however, that whereas the values of reduced χ^2 respond sensitively to small changes in T_{eff} and $[\text{Fe}/\text{H}]$, allowing for their optimal determinations, variations in the $\log g$ values do not strongly impact the reduced χ^2 , due to a lack of gravity-sensitive lines in the spectral window we examine. This leads to

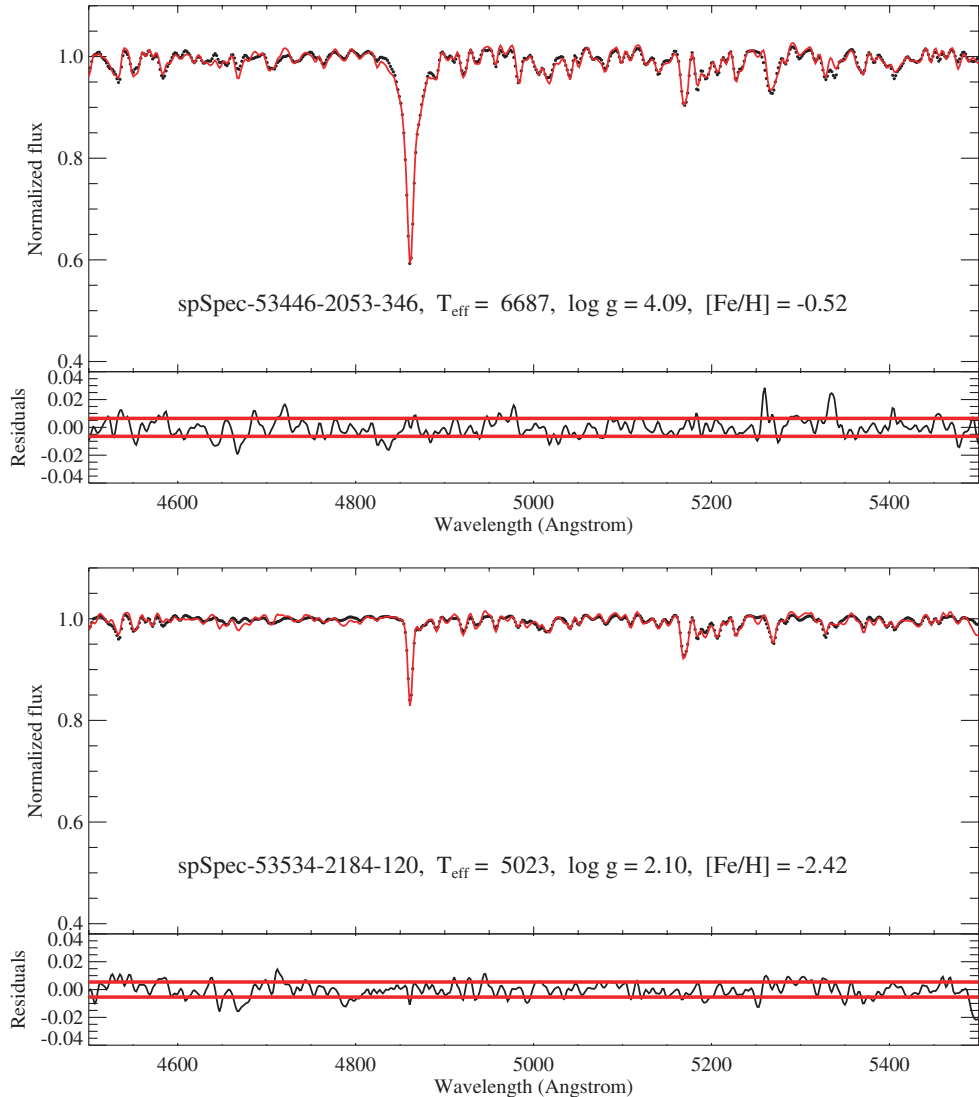


Figure 4. Two examples of the results of the application of the NGS1 grid, for a warmer, metal-rich star (top panel), and for a cooler, metal-poor star (bottom panel). The black dots are the observed data points; the red lines are synthetic spectra generated with the atmospheric parameters adopted by the technique. The residuals between the observed and synthetic spectra are also plotted at the bottom of each panel, with superimposed red lines representing the 1σ deviations of the residuals.

potentially large errors in the estimated $\log g$. This effect also appears in the function minimization techniques (e.g., Allende Prieto et al. 2006). We obtain a biweight average of the lowest 20 points of the reduced χ^2 values for the NGS1 grid, and 50 points for the NGS2 grid; the larger number of points included for the NGS2 grid is to accommodate the addition of an α -abundance parameter.

Figure 4 shows two examples of synthetic spectra (red lines) with parameters set to those estimated by the procedure described above, overplotted on the observed spectral data (black dots). The upper panel is for a warm, metal-rich main-sequence turn-off star; a cool metal-poor giant is shown in the bottom panel. The residuals between the observed and the synthetic spectra are plotted at the bottom of each panel; superimposed red lines show the standard deviation of the residuals to these fits.

4.4.4. Comparisons with Spectral Libraries and Analysis of High-Resolution SDSS-I/SEGUE Stars

In order to validate that the NGS1 and NGS2 grid approaches perform well in determining stellar parameter estimates, we compare the results from these techniques with literature values

from two spectral libraries: ELODIE (Prugniel & Soubiran 2001; Moulata et al. 2004) and MILES (Sánchez-Blázquez et al. 2006), as well as with parameter estimates from an analysis of the SDSS-I/SEGUE stars with available high-resolution spectroscopy.

Validation from the ELODIE and MILES Spectral Libraries

The spectra in the ELODIE library were obtained with the ELODIE spectrograph at the Observatoire de Haute-Provence 1.93 m telescope, and cover the spectral region 4000–6800 Å. We employ 1969 spectra of 1390 stars with a resolving power $R = 10,000$, which are publicly available as part of the ELODIE 3 release (Moulata et al. 2004). The spectra are first smoothed with a Gaussian kernel to match the SDSS resolution for the NGS2 grid and $R = 1000$ for the NGS1 grid, then are processed in the same fashion as described in Section 4.4.2. Most of the spectra have quite high-S/Ns, and are accompanied with estimated stellar parameters from the literature. Each spectrum (and parameter estimate) has a quality flag ranging from 0 to 4, with 4 being the best. In our comparison exercise, we select

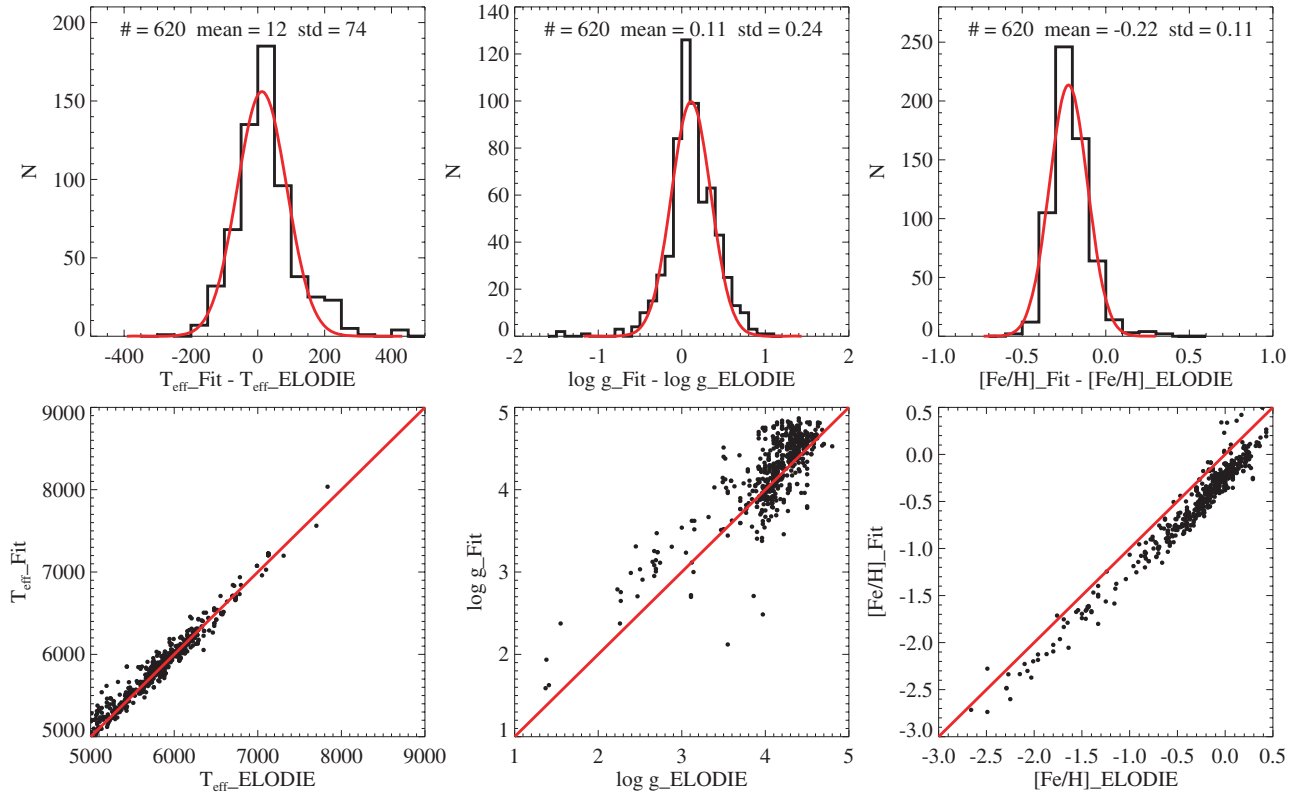


Figure 5. Comparison of parameters obtained from the NGS1 grid (FIT) with those from the ELODIE spectral library (ELODIE). The temperatures agree very well, while the surface gravity is overestimated by +0.11 dex. The metallicity is underestimated by −0.22 dex, but with a very small scatter, based on Gaussian fits to the residuals.

only stars with $4000 \text{ K} \leq T_{\text{eff}} \leq 10,000 \text{ K}$ with a quality flag ≥ 1 for the spectra and all of the parameters.

Our examination indicates that the NGS1 grid approach works best in the range $5000 \text{ K} \leq T_{\text{eff}} \leq 9000 \text{ K}$, and marginally well outside this range. Comparison plots between the literature values and the estimated parameters in this temperature range for 620 stars among the ELODIE spectral library are shown in Figure 5. A Gaussian fit to the residuals of each parameter reveals that the NGS1 estimate of T_{eff} is very close to the ELODIE zero point (offset by only 12 K), with a scatter of only 74 K; the surface gravity is larger by 0.11 dex ($\sigma = 0.24$ dex); the metallicity is lower by 0.22 dex ($\sigma = 0.11$ dex), on average. For cooler stars, with $4000 \text{ K} \leq T_{\text{eff}} \leq 5000 \text{ K}$, we find that $\langle \Delta(T_{\text{eff}}) \rangle$ and $\langle \Delta([\text{Fe}/\text{H}]) \rangle$ are 243 K ($\sigma = 91$ K) and 0.03 dex ($\sigma = 0.17$ dex), respectively, which are relatively small offsets and scatter, while the $\langle \Delta(\log g) \rangle$ is 0.45 dex, with $\sigma = 0.31$ dex.

Because the spectra from the ELODIE library are of very high quality, one might wonder how the parameter estimates would compare for the lower-S/N data included among the SDSS-I/SEGUE stars. In order to test this, we inject Gaussian noise into the ELODIE spectra to force them to $S/N = 50/1, 25/1, 12.5/1$, and $6.25/1$ per pixel at 5000 \AA , respectively, degrade them to $R = 1000$, and apply the same procedures as above for the estimation of the stellar atmospheric parameters.¹⁴ Table 4 lists the results of this exercise. Inspection of this table shows that, for $S/N \geq 12.5/1$, the shifts and scatter in the determinations of the parameters remain acceptably small.

The MILES library includes 985 spectra obtained with the 2.5 m INT and the IDS spectrograph at La Palma. The

wavelength coverage is 3530–7430 Å, and the resolution is $\sim 2.3 \text{ \AA}$ (Sánchez-Blázquez et al. 2006). We processed these spectra in the same manner as ELODIE to derive the stellar parameters from the NGS1 and NGS2 grids, but with no degradation of the spectra for the NGS2 grid, since the resolution is similar to that of the SDSS spectra. After dropping the spectra with missing parameters, or outside the temperature range $5000 \text{ K} \leq T_{\text{eff}} \leq 9000 \text{ K}$, 403 spectra remain. Figure 6 shows the comparison plots between the selected literature values and the parameters estimated from the NGS1 procedure. It appears that the scatter of the temperature ($\sigma = 120$ K) and the gravity ($\sigma = 0.31$ dex) estimates are higher than those from the ELODIE spectral library comparison, while the metallicity estimate is in good agreement ($\sigma = 0.17$ dex), except for a small negative offset (−0.24 dex). For the cooler stars, with $4000 \text{ K} \leq T_{\text{eff}} \leq 5000 \text{ K}$, we obtain $\langle \Delta(T_{\text{eff}}) \rangle = 235$ K with $\sigma = 130$ K, $\langle \Delta([\text{Fe}/\text{H}]) \rangle = -0.10$ dex with $\sigma = 0.17$ dex, and $\langle \Delta(\log g) \rangle = 0.45$ dex with $\sigma = 0.34$ dex.

Very similar behaviors were found for the comparison with the NGS2 grid technique as for the NGS1 grid technique, as listed in Table 4, which summarizes the offsets and scatter between the literature values and the estimated parameters for both synthetic grid approaches.

Validation from SDSS-I/SEGUE Stars with Available High-Resolution Spectra

As part of a long-term program to validate and improve estimates of stellar atmospheric parameters determined by the SSPP, over the past two years we have obtained higher-resolution spectra for over 150 SDSS-I and SEGUE stars. The targets cover a wide range of temperature and metallicity,

¹⁴ These test spectra, and more detailed information on noise models can be found at [ftp://hebe.as.utexas.edu/pub/callende/sdssim/](http://hebe.as.utexas.edu/pub/callende/sdssim/)

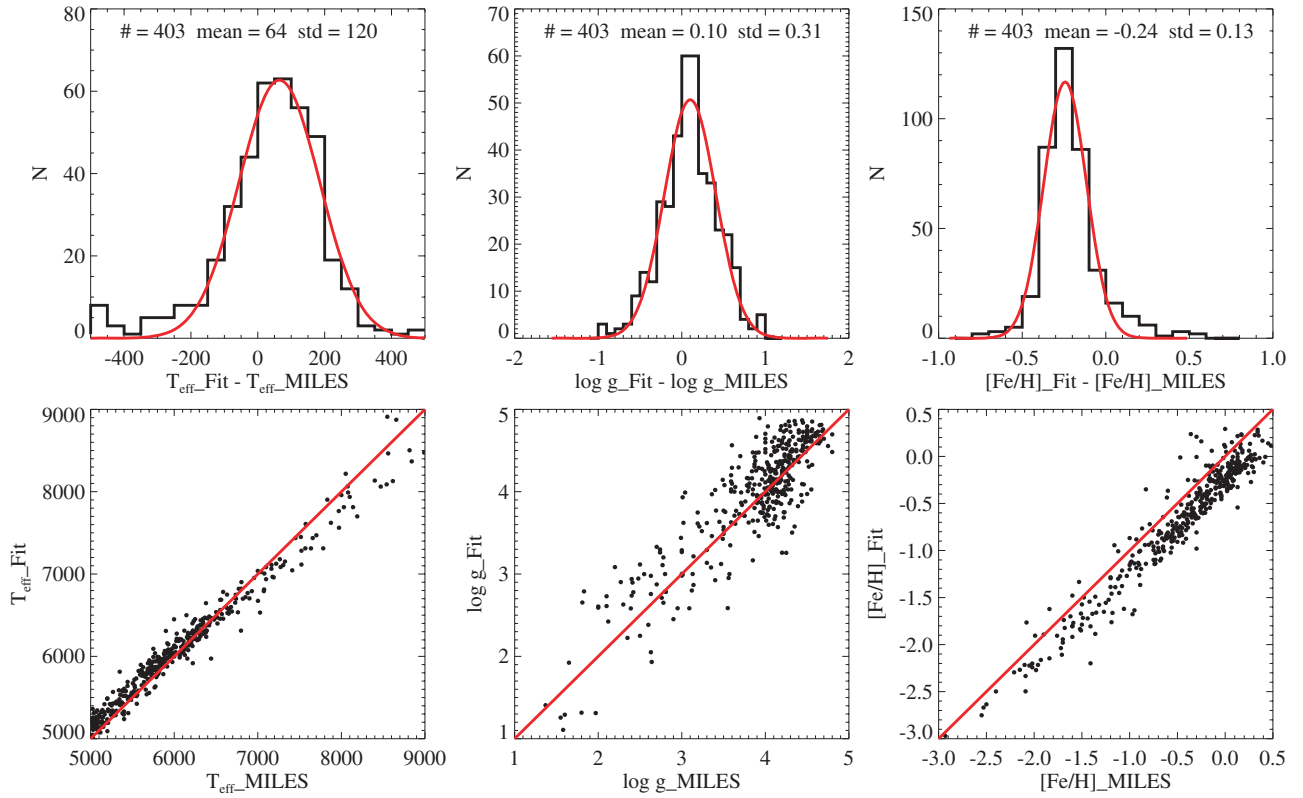


Figure 6. Comparison of parameters obtained from the NGS1 grid (FIT) with those from the MILES spectral library (MILES). The temperature and surface gravity are overestimated by +64 K and +0.10 dex, respectively, while the metallicity is underestimated by −0.24 dex, with a very small scatter, based on the Gaussian fits to the residuals.

but somewhat less so in surface gravity. Existing “holes” in the parameter space will be given high priority for future high-resolution campaigns. The data have been independently reduced and analyzed by two authors (C.A. and T.S.); we refer to the analysis by C.A. as HA1, and to that by T.S. as HA2, for a detailed description of these analyses, the interested reader is referred to Paper III in this series. For simplicity of our present comparison, we adopt the values of stellar atmospheric parameters obtained by HA1, which consists of a homogeneous sample (observed with the same telescope and spectrograph) of stars used to derive the empirical error estimates for the atmospheric parameters determined by the SSPP.

Figure 7 shows a comparison between the parameters estimated from the NGS1 grid approach and those determined from the HA1 high-resolution analysis, over $5000 \text{ K} \leq T_{\text{eff}} \leq 8000 \text{ K}$. As summarized in Table 4, the temperature and surface gravity estimates obtained from the NGS1 result in offsets of +85 K ($\sigma = 164 \text{ K}$) and +0.13 dex ($\sigma = 0.30 \text{ dex}$), respectively, which are somewhat larger than for the two spectral libraries. However, the average metallicity offset (−0.24 dex) and scatter (0.16 dex) are very close to those obtained by comparison with the two libraries. A similar behavior can also be noted for the NGS2 grid in Table 4.

Considering the results from these three different comparisons for the NGS1 and NGS2 grids, a small systematic offset in our derived metallicity and gravity from these two methods may exist. The slightly different offsets of the parameters between the two grids may come from the different resolutions employed. Therefore, we choose to adjust the offsets in $\log g$ by +0.11 dex and in [Fe/H] by −0.23 dex for the NGS1 method, and +0.16 dex and −0.24 dex for the NGS2 method, respectively,

in order to place those two grids on the same abundance scale, on average, as the two external libraries and the high-resolution analysis results. The offsets represent averages of those from the ELODIE, MILES, and HA1 comparisons.

The noise experiment summarized in Table 4, and another test (in Table 6, see Section 6 for details) indicate that a lower limit on S/N for obtaining useful parameter estimates from these two methods is, conservatively, $S/N \geq 15/1$ for the NGS1 approach, and $S/N \geq 20/1$ for the NGS2 approach. The color ranges we adopt for these techniques are $-0.3 \leq g - r \leq 1.3$ for the NGS1 approach, and $0.0 \leq g - r \leq 1.3$ for the NGS2 approach. The T_{eff} , $\log g$, and [Fe/H] estimated from the NGS1 approach are designated as T6, G6, and M6, respectively, whereas the $\log g$ and [Fe/H] estimated from the NGS2 technique are referred to as G7 and M7, respectively. No independent estimate of T_{eff} is obtained from the NGS2 grid, as is essentially degenerate with that determined from the NGS1 grid.

4.5. Metallicity and Gravity Estimates from 3850–4250 Å: CaIIK1 and CaI1

This method utilizes the NGS1 grid to estimate the metallicity and surface gravity, in a similar fashion as described in Section 4.4, but makes use of a different wavelength window: 3850–4250 Å. Even though it covers a relatively short wavelength region, it is desirable for the determination of stellar parameters because it includes the Balmer lines as temperature indicators, the metallicity-sensitive Ca II K and H lines, and the gravity sensitive Ca I (4226 Å) line. Comparisons with the results of the HA1 high-resolution analysis indicate an average zero-point offset in [Fe/H] of −0.06 dex, with a scatter of

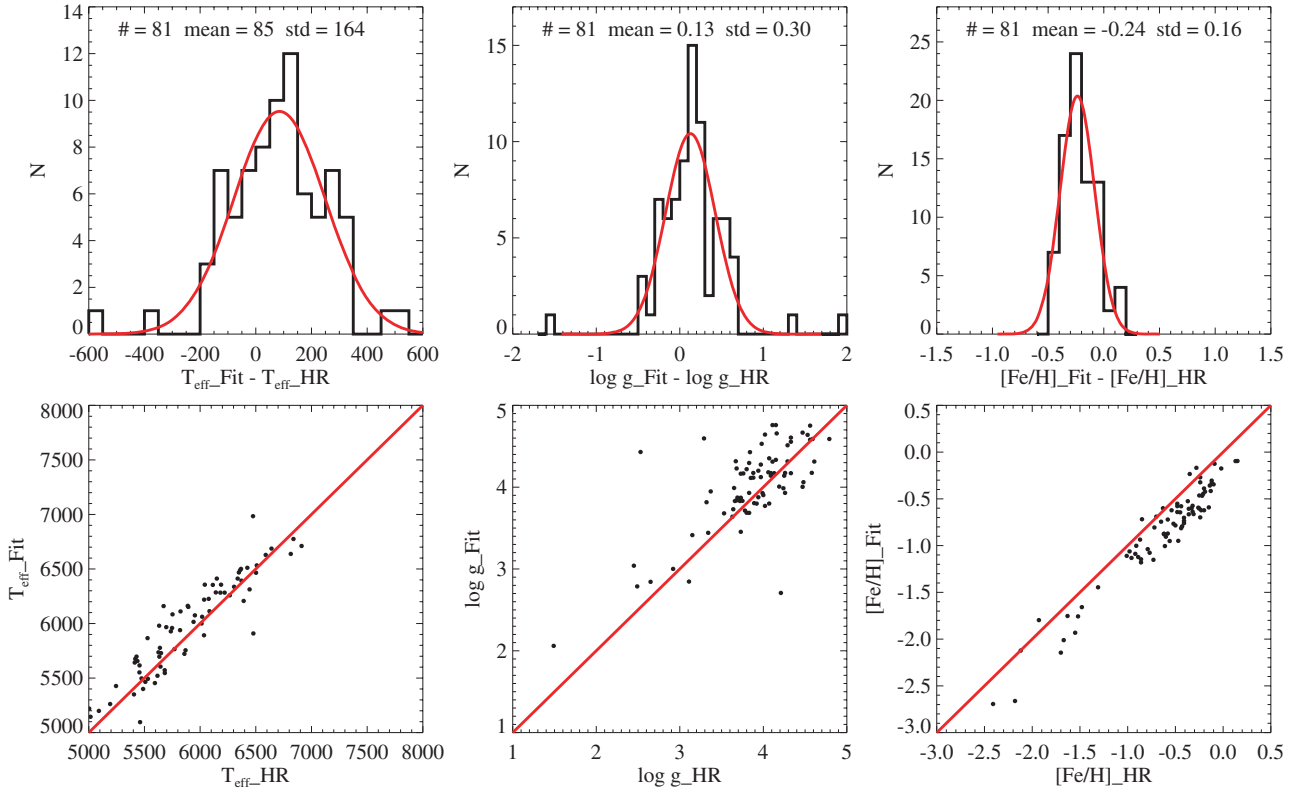


Figure 7. Comparison of parameters obtained from the NGS1 grid (FIT) with one of the analyses of high-resolution spectroscopy of SDSS-I/SEGUE stars (HR). The parameters for the high-resolution data are the HA1 results, which are used in Paper III to derive empirical errors of the SSPP parameters. The temperature exhibits a slightly higher offset than those from the comparisons with the ELODIE and MILES spectral libraries, but very similar offsets for the gravity and metallicity offsets.

0.25 dex, and an average zero-point offset in $\log g$ of +0.05 dex, and a scatter of 0.30 dex. The color range adopted for this approach is $-0.3 \leq g - r \leq 0.8$. The surface gravity and metallicity estimates obtained by this technique are referred to as G8 (CaII1) and M8 (CaIIK1), respectively.

4.6. The Ca II K and Autocorrelation Function Methods: CaIIK2, CaIIK3, and ACF

4.6.1. Metallicity from CaIIK2 and CaIIK3

These methods are based on the procedures outlined by Beers et al. (1999), to which we refer the interested reader for more details. A brief summary follows.

The Ca II K method, which is designated as CaIIK2, makes use of a “band-switched” estimate of the pseudo-equivalent of the Ca II K line at 3933 Å, in combination with an estimate of a broadband color, to obtain a prediction of the [Fe/H] for a given star. The approach has been used for two decades during the course of the HK (Beers et al. 1985, 1992) and the Hamburg/ESO objective prism surveys (Reimers & Wisotzki 1997; Christlieb 2003) for the determination of metallicities of stars with available medium-resolution (2–3 Å resolution, similar to the resolution of the SDSS spectra) follow-up spectroscopy. The original calibration is based on high-resolution abundance determinations (and $B - V$ colors) for a sample of ~ 500 stars.

This method has been shown to perform well over a wide range of metallicities, in particular for stars with $[Fe/H] < -1.0$; external errors from the calibration indicate that it has an intrinsic error no greater than 0.15–0.20 dex in the color range $0.3 \leq B - V \leq 1.2$. Above $[Fe/H] = -1.0$,

and in particular for cooler stars (below $T_{\text{eff}} = 5000$ K), the Ca II K line gradually begins to saturate. As a result, for cool, metal-rich stars, the method will generally return an estimate of [Fe/H] that is on the order of 0.5 dex too low. This is ameliorated somewhat by empirical corrections that are built into the program used to calculate this estimate, but it remains a source of concern. It is important to recognize that for stars with very low metallicities, and for warmer stars in particular, the Ca II K line is one of the few (in some cases only) metallic lines available in medium-resolution spectra. Hence, this estimator plays an especially important role in such situations.

This method makes use of a broadband $B - V$ color, which we have to obtain by application of a transformation of the observed (or predicted, as discussed in Section 5.2) $g - r$ colors. In order to accomplish this task, we made use of several hundred stars with existing $B - V$ colors obtained during the course of the HK and Hamburg/ESO surveys that happened to fall in the SDSS footprint, and had available $g - r$ colors (note that only the fainter, non-saturated stars could be used). These stars covered a variety of metallicities, but in particular a large number of stars with $[Fe/H] < -1.0$ were included. An approximate transformation, suitable for low-metallicity stars, was obtained by Zhao & Newberg (2006); the transform $B - V = 0.187 + 0.916(g - r)$ was employed.

The comparison of the metallicities obtained from the CaIIK2 method with those derived from the HA1 high-resolution analysis, and for member stars of open and globular clusters with known [Fe/H], indicates that the [Fe/H] for stars with $g - r > 0.8$ is consistently underestimated (due to the saturation of the Ca II K line).

As an alternative Ca II K-line approach, we have calibrated a new index, K24, which covers a broader region around the Ca II

Table 6
Parameter Sensitivities to Signal to Noise

Name	S/N	5		10		15		20		25		30		
		Method	$\langle \Delta \rangle$	σ										
T_{eff}														
Ad	Adop	-32.1	175.1	0.9	103.9	7.5	74.8	1.4	57.0	1.3	49.0	1.2	40.8	
T1	ki13	-0.1	316.0	-20.1	174.8	-8.9	119.3	-6.7	94.7	-5.9	72.6	-4.7	60.8	
T2	k24	-59.1	95.7	-39.5	74.8	-31.2	65.9	-24.7	54.2	-20.2	50.0	-14.2	43.2	
T3	WBG	4.7	12.1	4.5	9.9	4.7	8.9	4.4	8.8	4.4	8.2	4.5	7.8	
T4	ANNSR	225.3	676.5	142.5	343.2	69.0	199.4	30.6	143.6	24.2	115.8	23.7	106.1	
T5	ANNRR	-111.8	255.6	-13.3	154.9	19.5	106.1	24.7	78.8	27.2	62.9	23.2	51.5	
T6	NGS1	-11.7	315.8	-15.7	166.2	-4.5	117.3	-3.8	92.0	-3.3	75.3	-1.8	61.3	
T7	HA24	199.4	510.1	58.1	238.6	40.3	167.7	25.3	123.1	18.8	101.2	15.4	84.0	
T8	HD24	57.1	256.8	-29.7	155.5	-45.1	124.0	-52.6	97.7	-56.4	90.6	-56.6	86.7	
T9	T_K	
T10	T_G	
T11	T_I	
$\log g$														
Ad	Adop	-0.189	0.488	-0.112	0.282	-0.072	0.207	-0.067	0.168	-0.044	0.140	-0.038	0.127	
G1	ki13	-0.118	0.939	-0.071	0.507	-0.045	0.327	-0.040	0.277	-0.028	0.226	-0.021	0.191	
G2	k24	-0.200	0.627	-0.107	0.332	-0.079	0.269	-0.052	0.206	-0.044	0.175	-0.028	0.165	
G3	WBG	0.014	0.055	0.013	0.095	0.020	0.064	0.018	0.069	0.014	0.068	0.015	0.058	
G4	ANNSR	-0.535	1.044	-0.323	0.662	-0.156	0.424	-0.103	0.310	-0.071	0.236	-0.048	0.199	
G5	ANNRR	-0.081	0.235	-0.034	0.195	-0.009	0.150	0.001	0.122	0.014	0.111	0.013	0.092	
G6	NGS1	-0.079	0.942	-0.023	0.451	-0.021	0.313	-0.030	0.254	-0.022	0.203	-0.015	0.183	
G7	NGS2	-0.105	0.759	-0.052	0.402	-0.050	0.285	-0.056	0.228	-0.036	0.190	-0.032	0.161	
G8	CaI1	-0.037	0.680	-0.015	0.427	-0.023	0.325	-0.038	0.237	-0.030	0.202	-0.020	0.165	
G9	CaI2	-0.473	1.644	-0.054	0.758	-0.044	0.548	-0.035	0.428	-0.034	0.347	-0.018	0.279	
G10	MgH	-0.012	0.400	-0.031	0.226	-0.034	0.156	-0.021	0.122	-0.010	0.100	-0.006	0.087	
[Fe/H]														
Ad	Adop	0.141	0.476	0.059	0.213	0.050	0.144	0.025	0.102	0.009	0.082	0.005	0.074	
M1	ki13	0.515	0.565	0.172	0.254	0.111	0.182	0.071	0.148	0.041	0.116	0.027	0.091	
M2	k24	-0.019	0.371	-0.033	0.204	-0.015	0.148	-0.020	0.110	-0.017	0.099	-0.017	0.086	
M3	WBG	-0.272	0.405	-0.015	0.148	-0.011	0.074	0.016	0.057	0.016	0.056	0.016	0.056	
M4	ANNSR	0.203	0.860	-0.037	0.438	-0.028	0.317	-0.086	0.234	-0.120	0.162	-0.098	0.139	
M5	ANNRR	-0.029	0.375	-0.011	0.170	0.008	0.114	-0.002	0.086	-0.006	0.073	-0.008	0.062	
M6	NGS1	0.513	0.518	0.163	0.241	0.103	0.176	0.059	0.129	0.037	0.106	0.026	0.090	
M7	NGS2	0.533	0.580	0.246	0.268	0.227	0.199	0.142	0.149	0.096	0.115	0.067	0.099	
M8	CaKII1	0.210	0.517	0.062	0.324	0.046	0.226	0.026	0.153	0.010	0.131	0.005	0.107	
M9	CaKII2	-0.149	0.471	-0.036	0.195	0.017	0.114	0.023	0.074	0.026	0.065	0.025	0.057	
M10	CaKII3	-0.050	0.755	0.005	0.292	0.009	0.199	0.012	0.136	0.008	0.119	0.006	0.098	
M11	ACF	0.926	0.140	0.418	0.354	0.125	0.175	0.065	0.121	0.036	0.090	0.027	0.082	
M12	CaIIT	0.104	0.881	-0.040	0.822	-0.034	0.579	-0.034	0.487	-0.011	0.410	0.001	0.333	

Notes. $\langle \Delta \rangle$ is the average of the differences between the noise-added spectra and the original spectra; σ is the standard deviation of the differences. The temperature estimates T9, T10, and T11 do not change with S/N because they are computed from the $g - r$ color.

K line than the widest band considered for CaIIK2, and make use of the synthetic grids of predicted $g - r$ colors discussed above. Note that no “band switching” is used in this approach. A simplified neural network was designed to implement the prediction of [Fe/H] based on K24 and the synthetic $g - r$ color. As summarized in Table 10, this new calibration, which we refer to as CaIIK3, appears to exhibit similar (small) zero-point offsets and scatter as the CaIIK2 approach.

Due to concerns about the saturation of the Ca II K line for cooler stars, we consider only metallicities determined for stars using these two methods in the color range $0.1 \leq g - r \leq 0.8$. The parameters from these two approaches are referred to as M9 (CaIIK2) and M10 CaIIK3), respectively.

4.6.2. ACF

The autocorrelation function technique (ACF) was developed as an alternative method for metallicity estimation which

should perform well at higher metallicities, where the Ca II K line-index techniques described above are limited by saturation. As described in Beers et al. (1999), and references therein, the method relies on an autocorrelation of a given stellar spectrum, which generates a correlation peak whose strength is proportional to the frequency and strength of weak metallic lines in a given spectrum. The more such lines exist, the stronger the signal.

The calibration from Beers et al. (2000) relied on a broadband $B - V$ color. Encouraged by our success with the recalibration of the Ca II K approach to a (synthetic) native system $g - r$ color, we have designed a simple neural network that considers the autocorrelation function and the $g - r$ colors as inputs in order to predict [Fe/H].

The autocorrelation signal is expected to depend strongly on the S/N of a given spectrum, growing with decreasing S/N. In the low-S/N limit ($\leq 10/1$), this function is responding to

Table 7
Brief Descriptions of SSPP Flags

Position	Flag	Description	Category	Parameter
First	n	Appears normal	...	Yes
	D	Likely white dwarf	Critical	No
	d	Likely sdO or sdB	Critical	No
	H	Hot star with $T_{\text{eff}} > 10,000$ K	Critical	No
	h	Helium line detected, possibly very hot star	Critical	No
	l	Likely late type solar abundance star	Cautionary	Yes
	E	Emission lines in spectrum	Critical	No
	S	Sky spectrum	Critical	No
	V	No radial-velocity information	Critical	No
	N	Very noisy spectrum	Cautionary	Yes
Second	n	Appears normal	...	Yes
	C	The photometric $g - r$ color may be incorrect	Cautionary	Yes
Third	n	Appears normal	...	Yes
	B	Unexpected H α strength predicted from H δ	Cautionary	Yes
Fourth	n	Appears normal	...	Yes
	G	Strong G-band feature	Cautionary	Yes
	g	Mild G-band feature	Cautionary	Yes
Fifth	n	Appears normal	...	Yes
	P	Parameters reported for $5.0 \leq S/N < 10.0$	Cautionary	Yes
	N	No parameters	Critical	No
RV	NORV	No radial-velocity information	...	No
	ELRV	Radial velocity from ELODIE template	...	Yes
	BSRV	Radial velocity from <code>spectro1d</code>	...	Yes
	RVCAL	Radial velocity calculated from SSPP	...	Yes

Note. No parameters are reported when “Critical” flags are raised.

Table 8
Comparison of T_{eff} Estimates from Individual Methods with Those from Two High-Resolution Analyses

	Name Method	Ad Adop	T1 ki13	T2 k24	T3 WBG	T4 ANNSR	T5 ANNRR	T6 NGS1	T7 HA24	T8 HD24	T9 T_K	T10 T_G	T11 T_I
HA1	N	81	79	81	79	81	81	81	81	60	81	81	81
	$\langle \Delta \rangle$	+194	+142	+312	+230	+300	+179	+85	+139	+163	+125	+45	+146
	σ	182	231	249	196	197	182	164	142	147	295	252	268
HA2	N	125	120	120	116	122	125	125	123	96	125	125	125
	$\langle \Delta \rangle$	-32	-90	+46	-4	+36	-29	-140	-99	-74	-108	-178	-81
	σ	147	184	186	201	218	144	183	202	253	167	205	186
MEAN	N	125	120	120	116	122	125	125	123	95	125	125	125
	$\langle \Delta \rangle$	+64	-2	+136	+94	+132	+56	-37	+8	+43	-39	-83	-2
	σ	126	171	219	195	218	135	174	162	187	208	209	193

Notes. “Ad” is the adopted estimate of T_{eff} . HA1 indicates the analysis performed by C.A.; HA2 for T.S. MEAN is the average of the two analyses. “N” is the number of stars compared. $\langle \Delta \rangle$ is the mean zero-point offset from a Gaussian fit to the residuals of T_{eff} between the SSPP and the high-resolution analysis; σ is the standard deviation of the fit.

noise peaks rather than to the presence of metallic features. Our experiments with the sensitivity of abundance estimates on S/N (see Section 6) reflects this expectation. As can be seen from Table 6, the ACF approach exhibits a reasonably small zero-point offset (+0.13 dex) and scatter (0.18 dex) at

S/N levels as low as 15/1. We thus adopt this lower limit on S/N for determinations based on this method. The range of color adopted for the application of this method is taken to be $0.1 \leq g - r \leq 0.9$. Blueward of this range, the autocorrelation signal becomes too weak to be useful. Note that this range

Table 9
Comparison of $\log g$ Estimates from Individual Methods with Those from Two High-Resolution Analyses

	Name Method	Ad Adop	G1 ki13	G2 k24	G3 WBG	G4 ANNSR	G5 ANNRR	G6 NGS1	G7 NGS2	G8 CaI1	G9 CaI2	G10 MgH
HA1	N	81	79	81	79	80	81	81	80	77	32	35
	$\langle \Delta \rangle$	+0.02	+0.03	+0.06	-0.16	+0.01	+0.06	+0.06	+0.05	+0.05	+0.06	+0.04
	σ	0.21	0.34	0.33	0.69	0.25	0.22	0.30	0.29	0.30	0.30	0.26
HA2	N	125	120	120	116	118	123	122	120	117	47	51
	$\langle \Delta \rangle$	-0.02	-0.05	+0.00	-0.19	+0.01	+0.01	-0.01	-0.04	+0.00	-0.03	+0.00
	σ	0.33	0.44	0.43	0.82	0.45	0.37	0.41	0.39	0.37	0.40	0.24
MEAN	N	125	120	120	116	118	123	122	120	117	47	51
	$\langle \Delta \rangle$	+0.00	-0.01	+0.03	-0.19	+0.03	+0.02	+0.03	+0.01	+0.02	-0.00	+0.03
	σ	0.23	0.36	0.40	0.80	0.33	0.28	0.31	0.33	0.33	0.39	0.24

Table 10
Comparison of [Fe/H] Estimates from Individual Methods with Those from Two High-Resolution Analyses

	Name Method	Ad Adop	M1 ki13	M2 k24	M3 WBG	M4 ANNSR	M5 ANNRR	M6 NGS1	M7 NGS2	M8 CaKII1	M9 CaKII2	M10 CaKII3	M11 ACF	M12 CaIIT
HA1	N	81	53	56	47	49	62	64	45	53	29	31	30	34
	$\langle \Delta \rangle$	+0.02	+0.02	+0.02	+0.02	-0.02	-0.05	-0.02	-0.06	-0.00	+0.03	+0.06	+0.08	+0.06
	σ	0.15	0.14	0.14	0.19	0.13	0.16	0.14	0.12	0.24	0.24	0.20	0.19	0.22
HA2	N	125	80	82	63	70	102	97	73	84	46	56	43	52
	$\langle \Delta \rangle$	+0.04	+0.06	+0.10	+0.03	-0.00	-0.01	+0.03	+0.02	-0.02	+0.07	+0.02	+0.09	+0.22
	σ	0.33	0.27	0.33	0.38	0.31	0.28	0.28	0.26	0.38	0.38	0.43	0.37	0.31
MEAN	N	125	80	82	63	70	102	97	73	84	46	56	43	52
	$\langle \Delta \rangle$	+0.03	+0.05	+0.09	+0.01	-0.01	-0.03	+0.02	-0.01	-0.03	+0.03	-0.00	-0.00	+0.16
	σ	0.23	0.15	0.23	0.27	0.21	0.19	0.17	0.18	0.32	0.32	0.37	0.21	0.28

extends slightly redder than the Ca II K line-index methods. The [Fe/H] estimate from the ACF approach is referred to as M11.

4.7. Calibration of a Ca II Triplet Estimator of Metallicity: CaIIT

The SDSS spectra extend to sufficiently red wavelengths to include the prominent Ca II triplet feature, which covers the spectral region 8400–8700 Å. These lines are known to be sensitive to both luminosity (surface gravity) and metallicity, so care must be exercised in their use as a metallicity indicator.

We have employed a line index that measures the integrated strength of these lines, corrected for the presence of the Paschen Series H lines, which also occur in this wavelength interval. The line-index definition, and the calculation of the summed index, is as described by Cenarro et al. (2001a, 2001b). In order to calibrate this index for use with SDSS spectra, we have taken the library of some 700 spectra (and their listed atmospheric parameters) given by Cenarro et al.¹⁵ rebinned the spectra to the SDSS spectral resolution, and calculated the corrected Ca II triplet index (which they refer to as CAT'). This index, along with their listed de-reddened value of the $B - V$ color, are used as inputs to an artificial neural network procedure in order to predict the estimated [Fe/H]. This procedure was able to reproduce the metallicity of the Cenarro et al. stars to within ±0.3 dex over the temperature range 4000 K–8000 K, with some residual sensitivity to surface gravity. Clearly, the application of this approach would require a transform from $B - V$ to $g - r$, which we prefer to avoid.

Hence, we tested an approach that calibrated (with a simple neural network) the Cenarro et al. CAT' index along with synthetic $g - r$ colors, both obtained from the synthetic spectra described above. This approach appears to work reasonably well, as demonstrated by the inspection of the results shown in Table 10. The offsets and scatter obtained, relative to the high-resolution analyses, are quite competitive with other methods we have tested. However, it should be noted that the predicted sensitivity of this method to S/N is, according to the summary in Table 6, apparently somewhat high; although the zero-point offsets remain small, the scatter appears large compared with other methods (0.3–0.5 dex, even at $S/N \geq 20/1$). The results in Table 6 are obtained from the application of noise models for SDSS spectra (see Section 6), and we suspect that these may be imperfect in the red regions, or at least overaggressive, in the sense of injecting more noise than is typical for SDSS observations. We plan to investigate this behavior further in the near future.

The color range over which this estimate is employed by the SSPP is $0.1 \leq g - r \leq 0.7$. It may prove to be the case that we can set the red limit to larger values, once we understand the origin of the (apparently) large scatter obtained from the noise-injection test. For now, we set a conservative limit of $S/N \geq 20/1$ for application of this method. The [Fe/H] estimated from the CaIIT method is referred to as M12.

4.8. Calibration of a Gravity Estimator Based on the Ca I (4227 Å) and Mg I b and MgH Features: CaI2 and MgH

Among the prominent metallic species in stellar spectra, the two that are most sensitive to surface gravity are the Ca I line at 4227 Å and the Mg I b and MgH features around 5170 Å. Both

¹⁵ See <http://www.ucm.es/info/Astrof/ellipt/CATRIPLLET.html>

of these lines exhibit sensitivity to metallicity as well. We have adopted the line index measurements and quoted atmospheric estimates of [Fe/H] for the dwarfs and giants in the calibration sample of Morrison et al. (2003), which were measured at a similar spectral resolution to the SDSS (2.5–3.5 Å). Surface gravity estimates for the stars involved in this calibration were obtained from the compilation of Cayrel de Strobel et al. (2001), while $B - V$ colors were obtained from the SIMBAD database.

These indices, along with their de-reddened $B - V$ colors and [Fe/H], are used as inputs to an artificial neural network procedure in order to predict the estimated surface gravity $\log g$. This procedure indicates that the prediction errors of the surface gravity, based on the CaI and MgH indices are on the order of 0.35 dex and 0.30 dex, respectively. Small zero-point offsets, and similar levels of scatter, are indicated from the comparison with the high-resolution analyses in Table 10. Hence, we decided to proceed with these estimates (which require a color transformation), rather than attempt a recalibration to the synthetic spectra and colors.

As indicated by Morrison et al. (2003), these two methods are valid in the color range corresponding to $0.4 \leq g - r \leq 0.9$. The gravity estimated from CaI is referred to as G9 (CaI2), while that obtained from the MgH feature is referred to as G10 (MgH).

5. EMPIRICAL AND THEORETICAL PREDICTIONS OF T_{eff} AND $g - r$ COLOR

5.1. Predictions of T_{eff}

Effective temperatures predicted by the observed $g - r$ color, or through the strength of the Balmer lines, are sufficiently accurate to be considered as auxiliary estimators to those methods described in Section 4. We obtain two theoretical and three empirical temperature estimates during the execution of the SSPP.

5.1.1. Theoretical T_{eff} Estimates: T_K and T_G

Two theoretical temperature estimates are based on the NGS1 grid of synthetic spectra generated using the Kurucz models described in Section 4.4, and by consideration of predicted colors from the Girardi et al. (2004) isochrones. For the temperatures based on Kurucz models (T_K), we calculate an estimated $g - r$ color, adopting the SDSS filter and instrumental response functions (Strauss & Gunn 2001), then fit a fourth-order polynomial:

$$\begin{aligned} T_{\text{eff}} = & 7792.22 - 6586.18(g - r) - 4637.23(g - r)^2 \\ & - 1994.29(g - r)^3 - 386.24(g - r)^4. \end{aligned} \quad (4)$$

In deriving the above relationship, we take into account stellar models with atmospheric parameters in the range $-2.0 \leq [\text{Fe}/\text{H}] \leq -0.5$ and $3.0 \leq \log g \leq 5.0$, where most SDSS-I/SEGUE stars are found. Stars at the extrema of these ranges will have less than ideal estimates of temperature, due to the sensitivity of the $g - r$ color to either metallicity, surface gravity, or both. The effective temperature (T_K) estimated from this relation is referred to as T9.

For the temperature estimates based on the Girardi et al. isochrones (T_G), we assume that the stars are all older than 10 Gyr, are moderately metal poor (i.e., have metallicities in the range $-1.5 \leq [\text{Fe}/\text{H}] \leq -0.5$), and are subgiants or main-sequence stars, which is true for the great majority of the SDSS-

I/SEGUE stars. The temperature relationship, based on a third-order polynomial, is

$$\begin{aligned} T_{\text{eff}} = & 7590.26 - 6191.78(g - r) - 4270.92(g - r)^2 \\ & - 1225.12(g - r)^3. \end{aligned} \quad (5)$$

This temperature estimate (T_G) is referred to as T10.

5.1.2. Empirical T_{eff} Estimates: HA24, HD24, and T_l

Two of the three empirical temperature estimates we employ are derived from the Balmer-line strengths, similar to the color estimates discussed above, but calibrated to the effective temperature estimates obtained from the methods discussed in Section 4. The temperatures estimated from the HA24 and HD24 indices, via the simple linear relationships below, are referred to as T7 (HA24) and T8 (HD24), respectively.

$$T_{\text{eff}} = 4133 + 371 \cdot HA24 \quad (6)$$

$$T_{\text{eff}} = 5449 + 206 \cdot HD24. \quad (7)$$

We restrict the regions over which the above relationships are applied to $1.0 \text{ \AA} \leq HA24 \leq 12.0 \text{ \AA}$ and $1.0 \text{ \AA} \leq HD24 \leq 15.0 \text{ \AA}$, respectively. If the HA24 index lies the validity range, we adopt the T_{eff} estimate from HA24, and ignore the HD24 temperature estimate. If HA24 is out of range, we make use of the HD24 estimate of temperature.

The final empirical temperature estimate (T_l) comes from the relationship between the effective temperature derived from a previous version of the SSPP and the observed $g - r$ color (Ivezić et al. 2008). The temperature estimated from the relationship below is referred to as T11:

$$\begin{aligned} \log T_{\text{eff}} = & 3.8820 - 0.3160(g - r) + 0.0488(g - r)^2 \\ & + 0.0283(g - r)^3. \end{aligned} \quad (8)$$

It should be noted that T_K , T_G , and T_l are taken into account by the SSPP, provided that the color flag (see below) is not raised, and the expected temperature is beyond the region where the primary estimates derived from the techniques described in Section 4 apply. That is, they are used when the expected temperature is outside the range $4500 \text{ K} \leq T_{\text{eff}} \leq 7500 \text{ K}$.

5.2. Predictions of the $g - r$ Color

For a variety of reasons (e.g., nascent saturation, difficulties with de-blending of sources, high reddening, etc.), the SDSS PHOTO pipeline (Lupton et al. 2001) occasionally reports incorrect, or less-than-optimal, estimates of the broadband colors for a given target. Because several of the methods we employ in the SSPP require a good measurement of (at least) the $g - r$ color, it is useful to check if the reported $g - r$ color is commensurate with that predicted from the flux-calibrated spectrum of the source, or with the strength of spectral lines that correlate with effective temperature. This predicted color is used to raise a cautionary flag for stars with possibly incorrect reported colors, within some tolerance. We have developed three different methods to predict $g - r$ color in the SSPP, as described below.

5.2.1. Prediction of the $g - r$ Color from the Half Power Point Method

The first technique, the HPP method (Wisotzki et al. 2000), has been described in Section 4.4 above, in connection with

refining grid searches of parameter space. Here we obtain an empirical calibration of the $g - r$ color by fitting a functional relationship between the HPP wavelength of spectra for stars with well-measured SDSS colors and located in regions of high Galactic latitude, where reddening is minimal. The best-fit relationship is

$$g - r = -3.354 + 4.318 \cdot \text{HPP} + 3.247 \cdot \text{HPP}^2, \quad (9)$$

where $\text{HPP} = \lambda/10,000$. The expected error in prediction is about 0.08 mag over a broad range of colors.

The predicted color obtained in this fashion is (obviously) also a way to identify stellar spectra with poor spectrophotometric flux calibrations. If the observed color reported by the SDSS PHOTO routine is believed to be correct, and there remains a difference with the color obtained from the above relationship, one might be justifiably concerned about the quality of the spectrophotometric correction that has been applied. Unresolved binaries, especially those involving a red and a blue member, can also be identified by looking for discrepancies between the observed and predicted $g - r$ colors.

5.2.2. Prediction of the $g - r$ Color from the $H\delta$ and $H\alpha$ Lines

The strengths of the Balmer lines are also tightly correlated with $g - r$ color, over wide ranges of effective temperature. We have made use of the line indices for $H\delta$ and $H\alpha$, as determined by the SSPP, to obtain the following relationships:

$$g - r = 0.469 - 0.058 \cdot HD24 \quad (10)$$

and

$$g - r = 0.818 - 0.092 \cdot HA24, \quad (11)$$

where $HD24$ and $HA24$ are the $H\delta$ and $H\alpha$ line indices calculated over a 24 Å band centered on these lines. Note that since the $H\alpha$ line is stronger at a given color than the $H\delta$ line, it can be used to determine predictions of colors for cooler stars. The $H\alpha$ line is also located in a region of the spectrum where one expects generally fewer problems with contamination of the index from nearby metallic features.

6. THE IMPACT OF SIGNAL-TO-NOISE ON DERIVED ATMOSPHERIC PARAMETERS

Only the very brightest stars in the SDSS-I/SEGUE sample were accessible for follow-up high-resolution spectroscopic observations as part of the SEGUE calibration effort (see Paper III). Thus, the high-resolution data by themselves provide no information on the accuracy of the parameter estimates from the SSPP for SEGUE spectra with lower S/Ns (<about 30/1). To evaluate the accuracy and precision of the SSPP estimates of atmospheric parameters over a wide S/N range, we have developed a noise model for SEGUE data, applied it to the SDSS-I/SEGUE high-resolution calibration sample to create test spectra at many (more than 50) S/N values, and compare with the outputs of the SSPP, as run on these noise-added spectra, with the SSPP parameters determined from the original SEGUE spectra, and from the analysis of the high-resolution data.

The noise characteristics of SDSS-I/SEGUE data are modeled down to a lower limit of S/N per pixel of 5/1. These estimates are based on the extracted, flux-calibrated spectra and variance arrays from the SDSS/SEGUE spectroscopic reduction pipelines directly, not on the raw spectroscopic frames.

Each SDSS-I/SEGUE plug plate has spectroscopic targets that span the entire magnitude range of the bright or faint plug plates. The boundary between the faint and bright plug plates is set to $r \sim 18.0$. Since all targets on a given plug plate receive the same total exposure time, the relative contribution from the sky and object components of the noise changes over the magnitude range of the survey, with object noise dominant at high S/N and sky noise dominant at low S/N. The sky and stellar spectra have different spectral energy distributions, so in order to make a high-S/N SEGUE spectrum and its variance array resemble lower-S/N data, simply adding Poisson noise is not sufficient.

The noise model is constructed by measuring the ratio of the sky-to-object flux for a large subset of all the SEGUE spectra, 85,000 in the case of the tests described here, and parametrizing the mean value of that ratio and the width of the scatter about the mean versus S/N. This accounts for the increasing contribution from sky noise at lower S/N, and the range of the final S/N for targets at any magnitude because of variable conditions, etc. Then, to make a spectrum of any desired final S/N, the model uses that relation to scale the input spectrum and variance. The model then enforces equality between that ratio of sky-to-object flux and the ratio of the variances of the sky and object flux, since both the flux and variances should be proportional to the total counts. This deals with differences in how the reduction pipeline flux calibrations are applied to the sky and objects fibers and their variances. The model then randomly draws a sky residual spectrum from the set of all sky fibers on all the SEGUE plug plates and adds that zero-mean spectrum, now at the correct relative magnitude for the output S/N, to the noise-added data spectrum. We construct many (more than 50) realizations of each spectrum at each S/N value, each one with a different sky residual, and with the value used for the initial scaling of the input spectrum and its variance drawn as a Gaussian random deviate, described by the mean and scatter of the ratio of the sky-to-object flux in the survey data.

The end result is a noise-added spectrum for which the signal to noise versus wavelength is (as much as possible) indistinguishable from real data at a similar S/N. Our test spectra have S/N values ranging from 2.5/1 to 55/1. We have tested the noise-added spectra by checking the accuracy of the radial velocities for the test spectra versus S/N, and find good agreement with the accuracy as determined by comparing duplicate SEGUE observations that span the same range in S/N (C. Rockosi et al. 2008, in preparation). We have also measured the S/N at important spectroscopic features as blue as Ca II K versus the average S/N for the test spectra, and found good agreement with the same measurement for real spectra at similar $g - r$ colors.

From a sample of 108 calibration stars with \sim 450 different realizations in each S/N bin, we selected a subsample of spectra with 40 different realizations per bin, and examined how the stellar parameters determined by the methods used by the SSPP depend on S/N (over the range $5/1 \leq S/N \leq 30/1$). Table 6 summarizes the results. The S/N ratio is calculated by averaging over the spectral region 4000–8000 Å. Since we have numerous realizations of each spectrum at the same approximate S/N, we calculated the average S/N, as well as the mean offset and scatter of the parameters (compared to the non noise-injected spectra) by, e.g., selecting spectra with S/N between 3/1 and 7/1 for $S/N \sim 5/1$. The same procedure is applied to the other S/N regimes.

The S/N cuts we have chosen for the individual methods used by the SSPP (listed in Table 5) are based on this experiment.

The results for the temperature estimates T9, T10, and T11 are zeroed out in Table 6, because they are computed from the $g - r$ color alone.

7. FLAGS RAISED DURING THE EXECUTION OF THE SSPP

It is important that the SSPP be able to identify situations where the quoted atmospheric parameters may be in doubt, or simply to make the user aware of possible anomalies that might apply to a given star. We have designed a number of flags that serve this purpose.

There are two primary categories of flags—critical flags and cautionary flags. When a critical flag is raised, the SSPP is set to either ignore the determinations of atmospheric parameters for a given star, or it is forced (in the case of the color flag described below) to take steps that differ from normal processing in an attempt to rescue this information. Obviously, even when information is salvaged, the presence of a critical flag means the user must be aware that special steps have been taken, and the reported estimated parameters must be viewed with this knowledge in mind. The second category of the flags is the cautionary flags, which are provided for user consideration, but are not necessarily cause for undue concern. Indeed, sometimes these flags are raised when all is in fact fine, but the flag has been raised due to a peculiarity in the spectrum which is relatively harmless and will not unduly influence determination of atmospheric parameters. The user should nevertheless be aware of the existence of these flags.

The flags are combined into a single set of five letters, the meanings of which are summarized in Table 7, and described below in more detail. Five placeholders are used in order to accommodate cases where more than one sort of flag is raised.

The nominal condition for the five letter flag combination is “nnnnn,” which indicates that the SSPP is satisfied that a given stellar spectrum (and its reported $g - r$ colors and S/N) has passed all of the tests that have been performed, and the stellar parameters should be considered well determined.

The first letter in this combination is set to one of the ten different values: “n,” “D,” “d,” “H,” “h,” “I,” “E,” “S,” “V,” and “N.” Their explanations are as follows:

“n”—The letter “n” indicates nominal.

“D”—This flag is raised if a comparison of the breadth of the H δ line at 20% below its continuum, $D_{0.2}$, and the line depth below the continuum, R_c , relative to their expected relationship for “normal stars,” provided below, does not apply. The expected relationship is given by

$$R_c = -0.009503 + 0.027740 \cdot D_{0.2} - 0.000590 \cdot D_{0.2}^2 + 0.000006 \cdot D_{0.2}^3. \quad (12)$$

If $D_{0.2}$ is greater than 35.0 Å, and the predicted R_c from the above relationship is less than the measured value, then the star is most likely a white dwarf. This is a critical flag.

“d”—This flag is raised if $D_{0.2}$ is less than 35.0 Å, and the predicted R_c from above is less than the measured value. In this case, the star is most likely an sdO or sdB star. This is a critical flag.

“H”—This flag is raised when the estimated T_{eff} from the SSPP is greater than 10000 K, and is meant to indicate a hot star. This is a critical flag.

“h”—This flag is raised if the estimated T_{eff} from the SSPP is greater than 8000 K, and either of the line indices of He I (at 4026.2 Å) or He I (at 4471.7 Å) is greater than 1.0 Å. This indicates that the star is likely to be a hot star. This is a critical flag.

“I”—This flag is raised if the SSPP judges the star to have a high likelihood of being a late-type star (generally late K, M, or later spectral type), beyond the ability of the present pipeline to determine acceptable atmospheric-parameter estimates. The condition used for raising the “I” flag is that the Na line (5892.9 Å) index, as measured over a 24 Å band centered on this feature, is larger than 10 Å, and the $g - r$ color is greater than 0.8. This is a cautionary flag.

“E”—This flag is raised if significant emission lines are detected in a spectrum. This is a critical flag.

“S”—This flag is raised if the spectrum (according to the header information) is a night-sky spectrum. This is a critical flag.

“V”—This flag is raised when an adequate radial velocity could not be found for a given spectrum. This is a critical flag.

“N”—This flag is raised if the spectrum is considered noisy at the extremes of the wavelength range (e.g., around Ca II K and the Ca II triplet). This is a cautionary flag.

The flags that are used to fill out the remaining four positions of the five letter flag combination are “C,” “B,” “G,” “g,” “P,” and “N,” as described below. If none of these flags is raised, then the “n” flag is raised in their place:

“C”—This flag is raised if the SSPP is concerned that the reported $g - r$ color is incorrect. As mentioned above, we calculate three estimates of predicted $g - r$ colors, based on HA24, HD24, or the HPP method. For each of these three predicted colors, we find the one which is closest to the reported $g - r$ color based on the photometry. If the difference between the reported color and the closest predicted color is larger than 0.2 mag, the color flag (“C”) is raised. The SSPP is set up to proceed with its calculations of atmospheric parameters using the predicted $g - r$ color. This flag is always found in the second position of the combination flag parameters. This is a cautionary flag.

“B”—This flag is raised if the SSPP is concerned that there exists a strong mismatch between the strength of the predicted H α line index HA24, based on the measured H δ line index, HD24. For the great majority of “normal” stars, the predicted value of the H α line index is found to be $HA24 = 2.737 + 0.775 \cdot HD24$. For stars with significant HA24 and HD24 measurements (which we take to mean that the values of these indices exceed zero by more than 2σ , where σ is the error in the measured line index), if the difference between the predicted HA24 line index and the measured HA24 index is larger than 2.5 Å, then the “B” flag is raised. This flag is always found in the third position of the combination flag parameters. This is a cautionary flag.

“G or g”—This flag is raised if the SSPP suggests that the star may exhibit a strong (“G”) or mild (“g”) CH G-band (around 4300 Å), relative to expectation for “normal” stars. This flag is always found in the fourth position of the combination flag parameters. This is a cautionary flag.

“P or N”—This flag is raised in order to indicate if a spectrum either does (“n”), which is innocuous, or does not (“P”), which may be of concern, pass through the S/N cuts listed in Table 5, but still has an average S/N $\geq 5/1$. If no parameters are reported, or the average S/N $< 5/1$, the “N” flag is raised. The flag “P” is cautionary, while “N” is a critical flag.

8. THE SSPP DECISION TREE FOR FINAL PARAMETER ESTIMATION

The SSPP uses multiple methods in order to obtain estimates of the atmospheric parameters for each star over a very wide range in parameter space. Each technique has limitations as to its ability to estimate each parameter, arising from, e.g., the coverage of the grids of synthetic spectra, the methods used for spectral matching, and their sensitivity to the S/N of the spectrum, the range in parameter space over which the particular calibration used for a given method extends, etc. Hence, it is necessary to specify a prescription for the inclusion or exclusion of a given technique for the estimation of a given atmospheric parameter. At present, this is accomplished by the assignment of a null (0, meaning the parameter estimate is dropped), or unity (1, meaning the parameter estimate is accepted) value to an indicator variable associated with each parameter estimated by a given technique, according to the $g - r$ and S/N criteria listed in Table 5, and the flags that are raised. In the future, we plan to devise an improved weighting scheme for the combinations of the parameter estimates, once the grid of high-resolution spectroscopic determinations of atmospheric parameters is more completely filled out.

The S/N of a given spectrum plays a crucial role in the final decision as to the estimate of a set of atmospheric parameters, and the techniques used (which differ in their sensitivity to S/N). Table 5 lists the ranges of S/N where each particular method is considered valid. All derived parameters that fall outside of the color and S/N ranges listed in this table, for a given technique, are set to $T_{\text{eff}} = -9999$, $\log g = -9.999$, and $[\text{Fe}/\text{H}] = -9.999$, and have an indicator variable attached to a given parameter set to zero by the SSPP. However, if the S/N of a spectrum is greater than $5/1$, the parameters are saved (with the cautionary flag “P” raised).

Recall that in cases where the color flag “C” is raised, the predicted $g - r$ color determined by the procedures described above is used as an input (rather than the reported color) for the techniques that require this information.

8.1. Decisions on Effective Temperature Estimates

There are six primary temperature estimates determined by the SSPP, and an auxiliary set of five empirically and theoretically determined estimates. Note that a few of the primary techniques extend to temperatures below 4500 K and above 7500 K, although the accuracy obtained by these is lower than that in the interval $4500 \text{ K} < T_{\text{eff}} < 7500 \text{ K}$. Thus, for stars with temperatures outside of this interval, we also include the auxiliary temperature estimates (in fact, just those that lie within 3σ of the mean of the full auxiliary set) in assembling the final average estimate of T_{eff} . The averages are taken using the robust biweight procedure (see Beers et al. 1990, and references therein).

In cases where the color flag “C” is raised, we ignore all temperatures that rely on the reported $g - r$ color, and consider only those based on spectroscopy alone (e.g., the spectral-matching techniques and Balmer-line-based temperature). A

robust average of the accepted temperature estimates (those with indicator variables equal to 1) is taken for the final adopted temperature. An internal robust estimate of the scatter around this value is also obtained.

8.2. Decisions on Surface Gravity Estimates

There are ten methods used to estimate surface gravity by the SSPP. Application of the limits on $g - r$ and S/N eliminates a number of these estimates, and the biweight average of the accepted $\log g$ estimates (those with indicator variables equal to 1) is taken for the final adopted surface gravity. An internal robust estimate of the scatter around this value is also calculated.

8.3. Decisions on $[\text{Fe}/\text{H}]$ Estimates

Twelve different methods are employed to determine $[\text{Fe}/\text{H}]$ in the present SSPP. As before, indicator variables of 1 or 0 are assigned to the result from each method, according to whether or not it satisfies the range of validity listed in Table 5.

Rather than simply averaging the (accepted) metallicity estimates for each star, we have introduced a routine to identify and remove likely outliers. This involves the calculation of correlation coefficients between the observed and the synthetic spectra generated with the adopted temperature and gravity, and the individual estimates of the metallicity. Briefly, we start with the individual estimates of $[\text{Fe}/\text{H}]$ (with indicator variables of 1), the adopted T_{eff} , and $\log g$, and use these parameters to generate a synthetic spectrum by interpolating the pre-existing grid of the synthetic spectra (specifically the NGS1 grid). Then, we compute correlation coefficients between the observed and the generated synthetic spectra in two different wavelength regions: 3850–4250 Å and 4500–5500 Å, where the Ca II K and H lines, as well as numerous metallic lines, are present. We have avoided the region surrounding the CH G-band feature, as this molecular band can widely vary for stars with enhancements of carbon. Thus, for each estimator of $[\text{Fe}/\text{H}]$ there are two values of the correlation coefficient determined. We then select the region with correlation coefficient closest to unity. This applies for all estimates of $[\text{Fe}/\text{H}]$ from the individual methods. At the end of this process, we have N values of the correlation coefficient (maximum of $N = 12$) for the N estimates of $[\text{Fe}/\text{H}]$ with indicator variables of 1. After this, we take a robust average of the N values, and reject the values that are less than 1σ from the average. By application of this procedure, metallicity estimates that produce poor matches with the synthetic spectra are ignored, and are assigned indicator variables of 0. The final adopted value of $[\text{Fe}/\text{H}]$ is the biweight average of the remaining values of $[\text{Fe}/\text{H}]$ (those with indicator variables of 1). This procedure is followed for all stars with adopted temperatures $T_{\text{eff}} \geq 5000 \text{ K}$. For stars with adopted temperatures below this value, we do not consider the region 3850–4250 Å for the calculation of a correlation coefficient, because the Ca II K line is subject to saturation (and sometimes) the presence of line-core emission (due to an active chromosphere).

This procedure has been adopted after consideration of numerous alternative approaches for the final metallicity averaging. It appears to work (almost) as well as individual inspection by a trained spectroscopist, which would not be practical for the large numbers of spectra obtained by the SDSS.

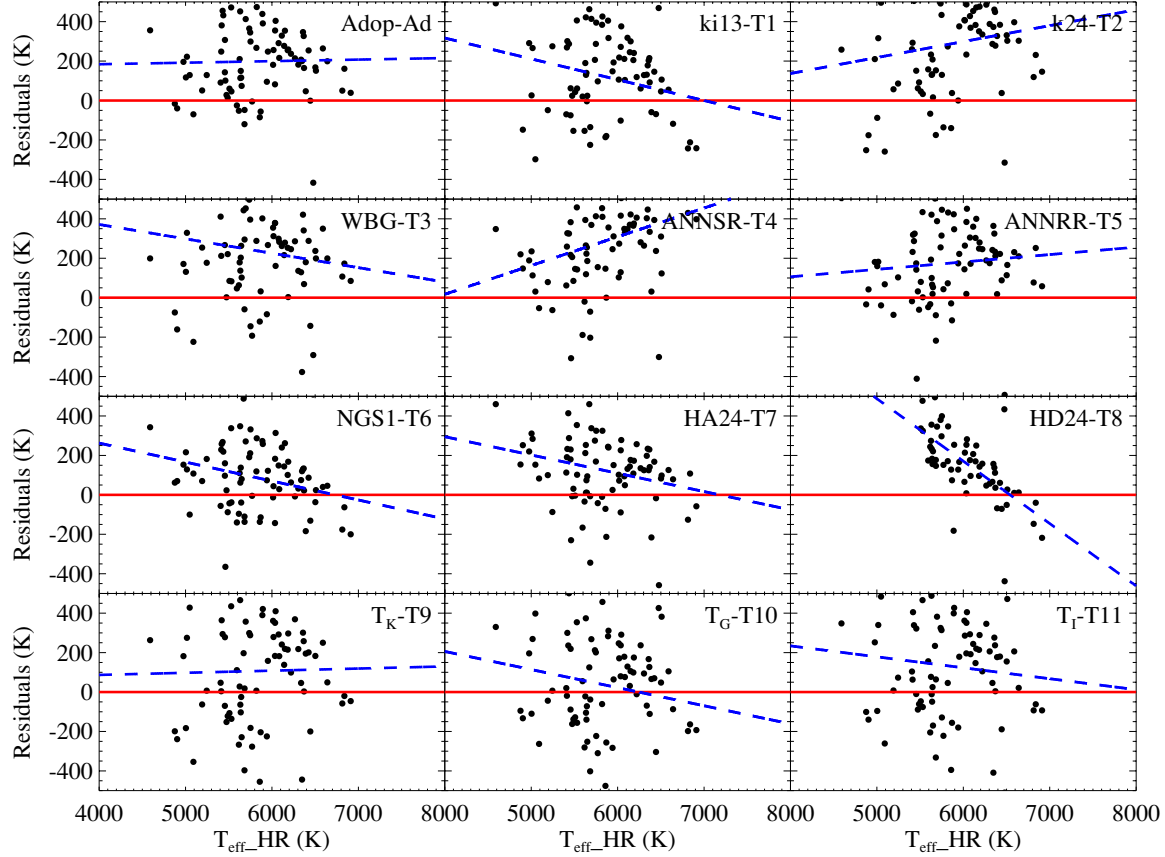


Figure 8. Comparison of effective temperatures estimated from individual methods with those from the HA1 high-resolution analysis of SDSS-I/SEGUE stars. “HR” indicates the (HA1) high-resolution analysis results. The residuals are the differences between the individual estimates and the high-resolution results. The red solid line is the zero point; the blue dashed line is a least-squares fit to the residuals.

9. VALIDATION OF THE FINAL SSPP PARAMETER ESTIMATES

We do not yet have at our disposal a completely satisfactory set of external spectral libraries, with suitable wavelength coverage and available atmospheric-parameter estimates, that extends over the full range of parameter space explored by techniques employed by the SSPP. Hence, we are limited to comparison with the sets of parameters obtained from analysis of the high-resolution spectra for SDSS-I/SEGUE stars obtained to date, and with information available from the literature for stars in Galactic open and globular clusters that have been observed during the course of the SDSS. Since Paper III focuses on the global uncertainties in the derived parameters from the SSPP, in this paper we concentrate on the comparison of individual methods with the results from the high-resolution analyses.

9.1. Validation from High-Resolution Spectroscopy

Table 2 summarizes the high-resolution data for SDSS-I/SEGUE stars obtained to date. Although the stars in this table cover most of the range explored by the SSPP techniques, there remain gaps in this coverage that we hope to fill in the near future.

As noted above, these data have been reduced and analyzed independently by two of the authors (C.A. and T.S.), making use of different methodologies. The details are discussed in Paper III. Tables 8–10 summarize the systematic offsets and scatters obtained for the estimates of T_{eff} , $\log g$, and $[\text{Fe}/\text{H}]$ from each of the techniques used by the SSPP, relative to high-

resolution analyses carried out individually and collectively. The differences in the numbers of stars considered independently arises because T.S. (results shown as HA2 in the tables) analyzed all available spectra, while C.A. (results shown as HA1 in the tables) performed analysis only for those stars observed with the HET. In the HA2 analysis, two different approaches were employed. The first is a routine that optimizes the minimum distances between the observed and synthetic spectra over a grid. This method was employed for the HET and Keck-ESI spectra. The second is the traditional high-resolution analysis approach, using Fe I and Fe II lines to constrain T_{eff} , $\log g$, $[\text{Fe}/\text{H}]$, and the microturbulence parameter. This approach was applied to the Keck-HIRES and Subaru-HDS data. More detailed explanations on the methods can be found in Paper III. The Keck-ESI, Keck-HIRES, and Subaru-HDS spectra with available parameters are defined as *OTHERS* in Paper III. In Paper III only the HET data analyzed by C.A. are used to derive the empirical random errors of the adopted parameters from the SSPP. However, in the present paper, we consider all available parameter estimates from all methods considered in the SSPP. The rows labeled MEAN in Tables 8–10 are the averaged results from HA1 and HA2 (for stars in common), supplemented with stars from HA2 where HA1 results were not obtained.

Figures 8–10 provide comparisons of the estimates of atmospheric parameters for individual techniques used by the SSPP with those obtained from the high-resolution analysis (HA1), for T_{eff} , $\log g$, and $[\text{Fe}/\text{H}]$, respectively.

The comparison of the estimated temperatures from the SSPP indicates, overall, very satisfactory results, although Table 8

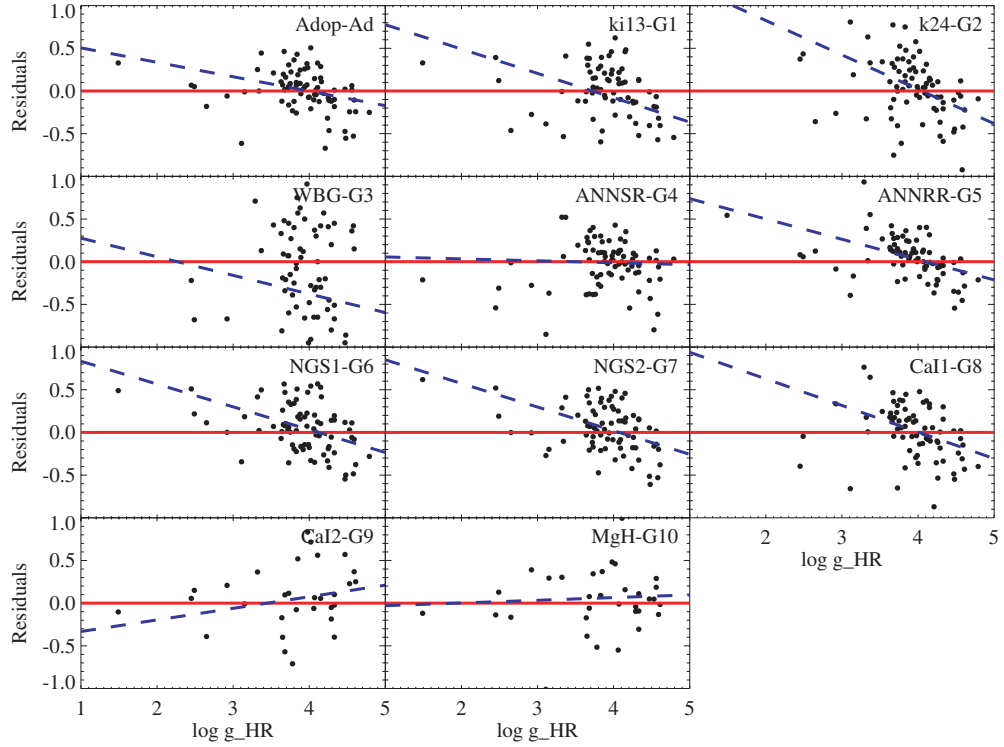


Figure 9. The same as Figure 8, but for the surface gravities, $\log g$.

reflects an interesting trend for T_{eff} ; estimates are mostly higher for the HA1 residuals, and mostly lower for HA2. However, as can also be noted from this table, the final adopted value of effective temperature from the SSPP exhibits a very small offset (+64 K) compared with the MEAN, and a 1σ scatter of 126 K, both of which are encouragingly small. It is clear from inspection of Figure 8 that additional high-resolution observations are required for stars with both higher and lower temperatures than the present sample. The distribution of the final adopted temperatures indicates no significant trends in the temperature range $4500 \text{ K} \leq T_{\text{eff}} \leq 7500 \text{ K}$, compared with the values from HA1, but there may exist a systematic offset of about 200 K.

Table 9 and Figure 9 for the surface gravity estimates reveal that the estimate G3 exhibits the highest offset, and largest scatter, relative to the high-resolution analyses, for reasons that are not presently clear. The residuals of the adopted values for surface gravity estimates from the SSPP are reasonably well distributed around zero for the high-gravity regime. High-resolution spectra for additional stars with lower surface gravities are required in order to confirm whether the slopes in the regression fits to the residuals for individual methods are real, or simply influenced by a few low-gravity stars. The mean offsets and 1σ scatters in the final adopted estimate of $\log g$ from the comparison with HA1 are +0.02 dex and 0.21 dex, respectively, and 0.00 and 0.23 dex for the MEAN comparisons. These are surprisingly good results for this difficult-to-estimate parameter.

It can be seen from Table 10 and Figure 10 that, except for M12, which exhibits a somewhat larger zero-point offset in HA2 and MEAN (but a small deviation from this zero point), all of the individual methods display satisfactorily small offsets with low scatter.

It is clear from inspection of Figure 10 that we could benefit from high-resolution analyses for more stars with intermediate metallicities, as well as for stars at the lowest metallicities. The

mean offset (+0.02 dex) and 1σ scatter (0.15 dex) of the residuals between the SSPP predictions of [Fe/H] and the high-resolution analysis (HA1) are quite encouraging, at least over the parameter space explored to date; the mean zero-point offset of +0.03 dex and scatter of 0.23 dex from MEAN is quite acceptable as well.

In summary, based on the sets of parameter comparisons with high-resolution analyses, in the effective temperature range of $4500 \text{ K} \leq T_{\text{eff}} \leq 7500 \text{ K}$, if we take the results from MEAN as “ground truth,” the SSPP is capable of producing estimates of the atmospheric parameters for SDSS-I/SEGUE stars to precisions of $\sigma(T_{\text{eff}})$, $\sigma(\log g)$, and $\sigma([\text{Fe}/\text{H}])$ of 141 K, 0.23 dex, and 0.23 dex, respectively, after adding systematic offsets quadratically. These uncertainties will be slightly reduced if we take into account the error contribution from the high-resolution analysis, as is done in Paper III. However, it should be kept in mind that the stars for which these comparisons are carried out are among the very brightest (high S/N > 50/1) observed with the SDSS, and the overall precision of parameter determination will slightly decline with S/N, as shown in Table 7.

Paper III takes a slightly different approach to derive empirical external errors of the parameters determined by the SSPP, and reports final external uncertainties of $\sigma(T_{\text{eff}}) = 130 \text{ K}$, $\sigma(\log g) = 0.21 \text{ dex}$, and $\sigma([\text{Fe}/\text{H}]) = 0.11 \text{ dex}$.

9.2. Validation from Galactic Open and Globular Clusters

Galactic open and globular clusters provide nearly ideal test beds for validation of the stellar atmospheric parameters estimated by the SSPP. In most clusters, it is expected that the member stars were born simultaneously out of well-mixed, uniform-abundance gas at the same location in the Galaxy. Therefore, the member stars should exhibit very similar elemental-abundance patterns. During the course of the SDSS-I and tests for SEGUE, we have secured photometric and spectroscopic data for the clusters M 13, M 15, M 2, NGC 2420, and M 67, and can make

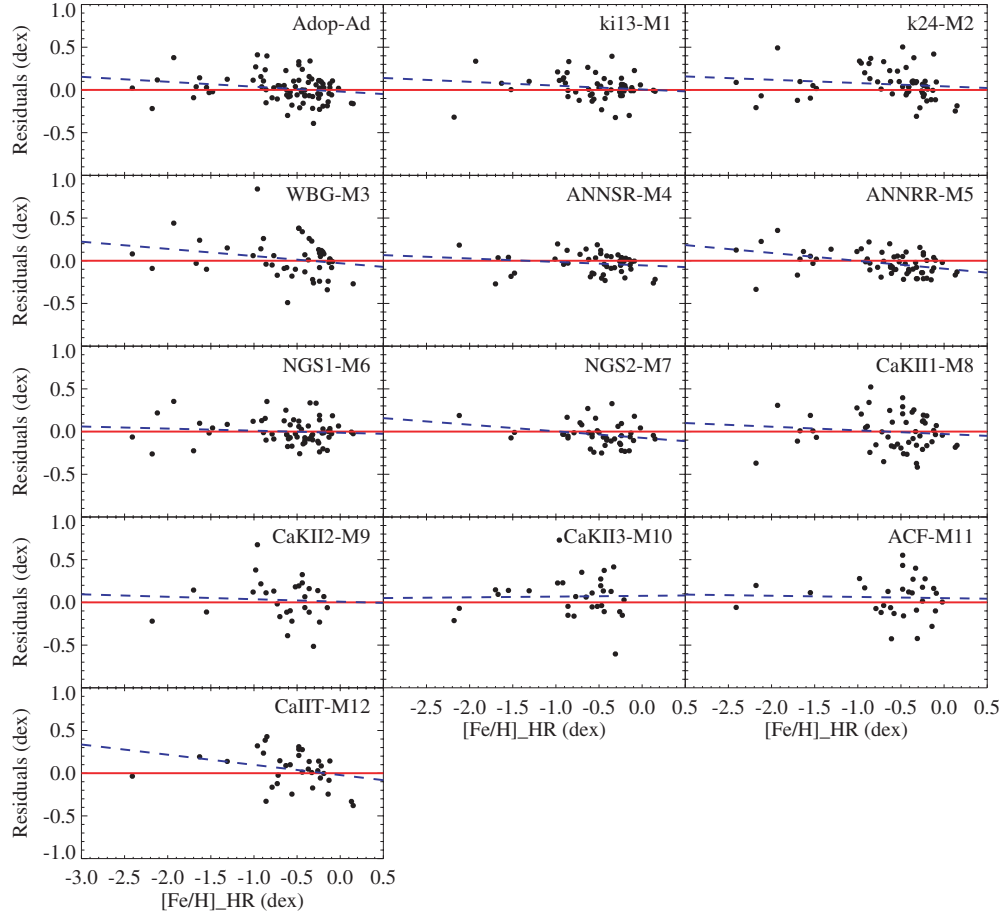


Figure 10. The same as Figure 8, but for the metallicities, [Fe/H].

use of these clusters for validation of the atmospheric parameters obtained by the SSPP. A more detailed description of this validation can be found in Paper II, to which we refer the interested reader. Here, we briefly report on just the results of the [Fe/H] comparisons as a function of the $g - r$ color and S/N.

Figure 11 shows, from top to bottom, the SSPP estimated metallicities for the selected member stars of M 15, M 13, M 2, NGC 2402, and M 67 as a function of $g - r$ color (left panels) and S/N (right panels). The solid red line is the literature value of metallicity, reported by Harris (1996), for M 15, M 13, and M 2, and Gratton (2000) for NGC 2402 and M 67, while the dashed green line indicates the mean SSPP estimate of [Fe/H] for the selected member stars. Inspection of this figure indicates that the overall mean [Fe/H] values obtained from the SSPP generally agrees, within 0.1 dex, with the literature values. In addition, there is no noticeable trend with $g - r$ or S/N, which indicates that reliable estimates of [Fe/H] are produced by the SSPP for a wide range of spectral types and S/N. Observations of clusters with intermediate metallicity, which would fill the gap in metallicity space, will clearly be helpful for future tests of the SSPP.

10. ASSIGNMENT OF SPECTRAL CLASSIFICATIONS FOR EARLY AND LATE-TYPE STARS

It is often useful to group stars into rough MK spectral classifications. It should be kept in mind, however, that for this, and any other exercise of assigning MK spectral types, that the MK system *does not apply* to stars other than Population I. That

is, typing of metal-poor Population II stars is, *by definition*, not a strictly valid procedure. Nevertheless, the SSPP attempts to carry out this exercise using two approaches. The first is based on the spectral type listed in the ELODIE database for the best template match obtained for the determination of radial velocity (as described above), and applies to stars with spectral classes O to M.

For the coolest stars, measurement of accurate values of T_{eff} , $\log g$, and [Fe/H] from spectra dominated by broad molecular features becomes extremely difficult (e.g., Woolf & Wallerstein 2006). As a result, the SSPP does not estimate atmospheric parameters for stars with $T_{\text{eff}} < 4000$ K, but instead estimates the MK spectral type of each star using the “Hammer” spectral-typing software developed and described by Covey et al. (2007).¹⁶ The Hammer code measures 23 spectral indices, including atomic lines (H, Ca I, Ca II, Fe I, Mg I, Na I) and molecular band heads (CN, G-band, TiO, VO, CaH, FeH), as well as a select set of broadband color ratios. The best-fit spectral type of each target is assigned by comparison to the grid of indices measured from more than 1000 spectral-type standards derived from spectral libraries of comparable resolution and coverage (Allen & Strom 1995; Prugniel & Soubiran 2001; Hawley et al. 2002; Bagnulo et al. 2003; Le Borgne et al. 2003; Valdes et al. 2004; Sánchez-Blázquez et al. 2006).

Tests of the accuracy of the Hammer code with degraded ($S/N \sim 5/1$) STELIB (Le Borgne et al. 2003), MILES

¹⁶ The Hammer has been made available for community use: the IDL code can be downloaded from <http://www.cfa.harvard.edu/kcovey/>

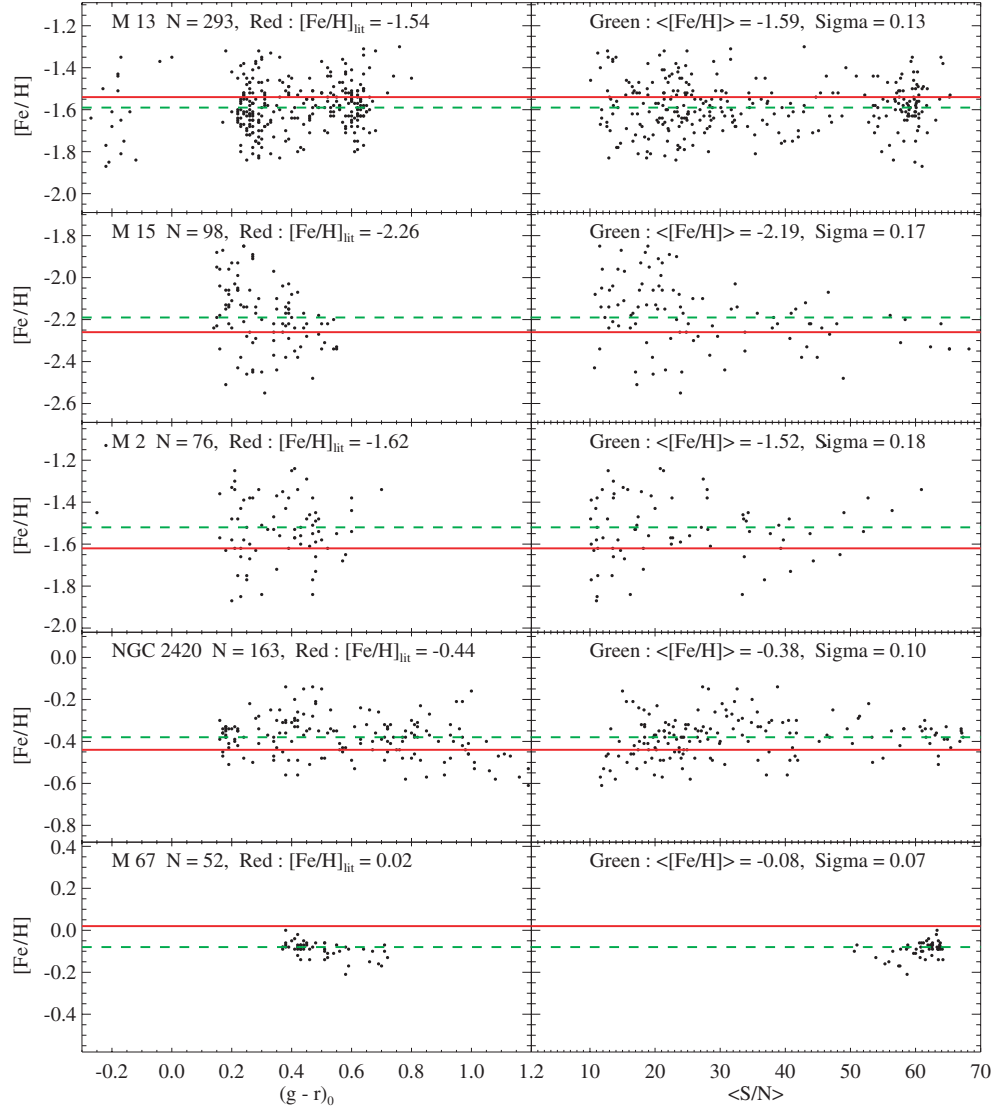


Figure 11. SSPP-estimated metallicities with respect to $g - r$ (left panels) and S/N (right panels) for the selected member stars of M 15, M 13, M 2, NGC 2420, and M 67. See Paper II for a more detailed discussion of the selection of member stars. The green dashed line is the average metallicity ($\langle [\text{Fe}/\text{H}] \rangle$) of the selected member stars of each cluster. The red line is the adopted literature value ($[\text{Fe}/\text{H}]_{\text{lit}}$). Metallicities for M 15, M 13, and M 2 are taken from Harris (1996); NGC 2420 and M 67 are from Gratton (2000). The total number (N) of the selected member stars is also indicated; sigma is the standard deviation of the residuals about the SSPP adopted value.

(Sánchez-Blázquez et al. 2006), and SDSS (Hawley et al. 2002) dwarf template spectra reveal that the Hammer code assigns spectral types accurate to within ± 2 subtypes for K and M stars. The Hammer code also returns results for warmer stars, but as the set of indices used is optimized for cool stars, typical uncertainties are ± 4 subtypes for A-G stars at $S/N \sim 5/1$; in this temperature regime, the SSPP atmospheric parameters are a more reliable indicator of T_{eff} .

Given the science goals of, in particular, the SEGUE program, we emphasize two limitations to the accuracy of spectral types derived by the Hammer code:

1. The Hammer code uses spectral indices derived from dwarf standards; spectral types assigned to giant stars will likely have larger, and systematic uncertainties.
2. The Hammer code was developed in the context of SDSS-I's high Galactic latitude spectroscopic program; the use of broadband color ratios in the indices will likely make the spectral types estimated by the Hammer code particularly sensitive to reddening. Spectral types derived in areas

of high extinction (i.e., low-latitude SEGUE plug plates) should be considered highly uncertain until verified with reddening-insensitive spectral indices.

11. DISTANCE ESTIMATES

A number of techniques are presently being explored by members of the SEGUE team in order to derive the best-available estimates of distances for stars in the SDSS/SEGUE database. Many rely on the existence of either theoretical or empirical transformations of the substantial amount of photometric data that exists for Galactic clusters obtained with photometric systems other than $ugriz$. An et al. (2008) have recently reported accurate globular and open cluster fiducials for a set of 20 clusters observed by the SDSS, making use of crowded-field photometric measurements. We expect to revise the distance estimates obtained by the SSPP, based on this work, in the near future.

For now, the SSPP assigns preliminary distance estimates for stars of different luminosity classifications based on the

empirical fits of Beers et al. (2000) to the observed color-magnitude diagrams of Galactic clusters of different metallicities and with reasonably well-known distances (in the Johnson $V, B - V$ system). For convenience, we use the same transformations as mentioned above, based on the work of Zhao & Newberg (2006); $V = g - 0.561(g - r) - 0.004$, and $B - V = 0.187 + 0.916(g - r)$.

Beers et al. (2000) argue that their distances should be accurate to on the order of 10–20%; a typical value of 15% can be adopted for our distance estimates, although this needs to be confirmed with future work.

The SSPP does *not* make a stellar luminosity classification, but rather, it provides the atmospheric parameters from which the user can make an appropriate choice. Distance estimates are obtained for the following rough luminosity classes: dwarf, main-sequence turnoff, giant, asymptotic giant branch, and field horizontal-branch. Note that the distance estimates are obtained for all (feasible) cases where a star may fall into one or more of these classifications, but only one of the listed distances is likely to apply to a given star. The choice is left up to the user.

An alternative method for distance estimates in the SSPP is described by Allende Prieto et al. (2006), to which the interested reader is referred for a detailed description.

12. SUMMARY

We have described the development and execution of the SSPP, which makes use of multiple approaches in order to estimate the fundamental stellar atmospheric parameters (effective temperature, T_{eff} , surface gravity, $\log g$, and metallicity, parameterized by [Fe/H]) for stars with spectra and photometry obtained during the course of the original SDSS-I and its current extension (SDSS-II/SEGUE).

The use of multiple approaches allows for an empirical determination of the internal errors for each derived parameter, based on the range of the reported values from each method. Among 128,000 spectra from 200 SEGUE plug plates, typical internal errors for stars which have derived stellar parameters available, from the SSPP, in the range $4500 \text{ K} \leq T_{\text{eff}} \leq 7500 \text{ K}$, are $\sigma(T_{\text{eff}}) = 70 \text{ K}$ (s.e.m.), $\sigma(\log g) = 0.18$ (s.e.m.), and $\sigma([\text{Fe}/\text{H}]) = 0.07$ (s.e.m.). Paper III points out that the internal scatter estimates obtained from averaging the multiple estimates of the parameters produced by the SSPP underestimate the external errors, owing to the fact that several methods in the SSPP use similar parameter indicators and atmospheric models.

The results of a comparison with an average of two different high-resolution spectroscopic analyses of over 100 SDSS-I/SEGUE stars suggests that the SSPP is able to determine T_{eff} , $\log g$, and [Fe/H] to precisions of 141 K, 0.23 dex, and 0.23 dex, respectively, after combining small systematic offsets quadratically for stars with $4500 \text{ K} \leq T_{\text{eff}} \leq 7500 \text{ K}$. These errors differ slightly from those obtained by Paper III ($\sigma(T_{\text{eff}}) = 130 \text{ K}$, $\sigma(\log g) = 0.21$ dex, and $\sigma([\text{Fe}/\text{H}]) = 0.11$ dex), even though they share a common set of high-resolution calibration observations. This arises because Paper III derived the external uncertainties of the SSPP only taking into account the stars observed with the HET (on the grounds of internal consistency). The sample referred to as *OTHERS* in Paper III exhibits somewhat larger scatter in its parameters, when compared with those determined by the SSPP. Observation of several hundred additional stars from SDSS-I/SEGUE with the HET is now underway. Thus, in the future, we will be able to use a homogeneous sample

gathered by the HET in our tests. Also, additional high-resolution data for stars outside our adopted temperature range will enable tests for both cooler ($T_{\text{eff}} < 4500 \text{ K}$) and warmer ($T_{\text{eff}} > 7500 \text{ K}$) stars.

Considering the average internal scatter from the multiple approaches and the external uncertainty from the comparisons with the high-resolution analysis together, the typical uncertainty in the stellar parameters delivered by the SSPP are $\sigma(T_{\text{eff}}) = 157 \text{ K}$, $\sigma(\log g) = 0.29$ dex, and $\sigma([\text{Fe}/\text{H}]) = 0.24$ dex, over the temperature range $4500 \text{ K} \leq T_{\text{eff}} \leq 7500 \text{ K}$.

However, it should be kept in mind that the errors stated above apply for the very highest S/N spectra obtained from the SDSS ($S/\text{N} > 50/1$), as only quite bright stars were targeted for high-resolution observations. The uncertainty of the parameter estimates will be larger, with declining S/N, as shown in Table 6. In addition, outside the quoted temperature range ($4500 \text{ K} \leq T_{\text{eff}} \leq 7500 \text{ K}$), we presently do not have sufficient high-resolution spectra to fully test the parameters obtained by the SSPP.

The results of a comparison to literature values of the overall [Fe/H] of selected member stars in a sample of Galactic open and globular clusters suggests that the metallicities estimated by the SSPP are within ± 0.1 dex of these values, for a wide range of colors ($-0.3 \leq g - r \leq 1.3$), down to a spectroscopic S/N of 10/1. This analysis implies that the valid range of the effective temperature for determining the stellar parameters by the SSPP is wider than that presently testable with the high-resolution analysis. Once we obtain high-resolution spectroscopy of hot ($T_{\text{eff}} > 7500 \text{ K}$) and cool ($T_{\text{eff}} < 4500 \text{ K}$) stars, we will be able to better confirm the color range where the SSPP is capable of estimating accurate parameters.

Approximate spectral types are assigned for stars, based on two methods, with differing limitations. A set of distance determinations for each star is also obtained, although future work will be required in order to identify the optimal method.

We conclude that the SSPP determines, with sufficient accuracy and precision, radial velocities and atmospheric-parameter estimates, for stars in the effective temperature range from 4500 K to 7500 K, to enable detailed explorations of the chemical compositions and kinematics of the disk and halo populations of the Galaxy.

Funding for the SDSS and SDSS-II has been provided by the Alfred P. Sloan Foundation, the Participating Institutions, the National Science Foundation, the U.S. Department of Energy, NASA, the Japanese Monbukagakusho, the Max Planck Society, and the Higher Education Funding Council for England. The SDSS Web site is <http://www.sdss.org/>.

The SDSS is managed by the Astrophysical Research Consortium for the Participating Institutions. The Participating Institutions are the American Museum of Natural History, Astrophysical Institute Potsdam, University of Basel, University of Cambridge, Case Western Reserve University, University of Chicago, Drexel University, Fermilab, the Institute for Advanced Study, the Japan Participation Group, Johns Hopkins University, the Joint Institute for Nuclear Astrophysics, the Kavli Institute for Particle Astrophysics and Cosmology, the Korean Scientist Group, the Chinese Academy of Sciences (LAMOST), Los Alamos National Laboratory, the Max-Planck-Institute for Astronomy (MPIA), the Max-Planck-Institute for Astrophysics (MPA), New Mexico State University, Ohio State

University, University of Pittsburgh, University of Portsmouth, Princeton University, the United States Naval Observatory, and the University of Washington.

Y.S.L., T.C.B., and T.S. acknowledge partial funding of this work from grant PHY 02-16783: Physics Frontiers Center/Joint Institute for Nuclear Astrophysics, awarded by the U.S. National Science Foundation. NASA grants (NAG5-13057, NAG5-13147) to C.A. are gratefully acknowledged. J.E.N. acknowledges support from Australian Research Council Grant DP0663562. C.B.J. and P.R.F. acknowledge support from the Deutsche Forschungsgemeinschaft (DFG) grant BA2163. Support through the Marie Curie Research Training Network European Leadership in Space Astrometry under contract MRTN-CT-2006-033481 to P.R.F. is also acknowledged. H.Z. and A.L.L. acknowledge partial support from the Chinese Academy of Sciences (LAMOST).

REFERENCES

- Abazajian, K., et al. 2003, *AJ*, **126**, 2081
 Abazajian, K., et al. 2004, *AJ*, **128**, 502
 Abazajian, K., et al. 2005, *AJ*, **129**, 1755
 Adelman-McCarthy, J. K., et al. 2006, *ApJS*, **162**, 38
 Adelman-McCarthy, J. K., et al. 2007, *ApJS*, **172**, 634
 Adelman-McCarthy, J. K., et al. 2008, *ApJS*, **175**, 297
 Allen, L. E., & Strom, K. M. 1995, *AJ*, **109**, 1379
 Allende Prieto, C., et al. 2006, *ApJ*, **636**, 804
 Allende Prieto, C., et al. 2008, *AJ*, **136**, 2070 (Paper III)
 Alvares, R., & Plez, B. 1998, *A&A*, **330**, 1109
 An, D., et al. 2008, *ApJS*, in press (arXiv:0808.0001)
 Asplund, M., Grevesse, N., & Sauval, A. J. 2005, in ASP Conf. Ser. 336, Cosmic Abundance as Records of Stellar Evolution and Nucleosynthesis, eds. T. G. Barnes III, & F. N. Bash (San Francisco, CA: ASP), 25
 Bagnulo, S., et al. 2003, The Messenger, **114**, 10
 Barklem, P. S., & O'Mara, B. J. 1998, *MNRAS*, **300**, 863
 Beers, T. C., Flynn, K., & Gebhardt, C. 1990, *AJ*, **100**, 32
 Beers, T. C., Preston, G. W., & Shectman, S. A. 1985, *AJ*, **90**, 2089
 Beers, T. C., Preston, G. W., & Shectman, S. A. 1992, *AJ*, **103**, 1987
 Beers, T. C., Rossi, S., Norris, J. E., Ryan, S. G., & Shefler, T. 1999, *ApJ*, **506**, 892
 Beers, T. C., et al. 2000, *AJ*, **119**, 2866
 Beers, T. C., et al. 2007, *AAS*, **211**, 1427
 Castelli, F., Gratton, R. G., & Kurucz, R. L. 1997, *A&A*, **318**, 841
 Castelli, F., & Kurucz, R. L. 2003, IAU Symp. 210, Modelling of Stellar Atmospheres, ed. N. Piskunow, W. W. Weiss, & D. F. Gray (Dordrecht: Kluwer), A20
 Cayrel, R. 1988, IAU Symp. 132, The Impact on Very High S/N Spectroscopy on Stellar Physics ed. G. Cayrel de Strobel & M. Spite (Dordrecht: Kluwer), 345C
 Cayrel de Strobel, G., Soubiran, C., & Ralite, N. 2001, *A&A*, **373**, 159
 Cenarro, A. J., Cardiel, N., Gorgas, J., Peletier, R. F., Vazdekis, A., & Prada, F. 2001a, *MNRAS*, **326**, 959
 Cenarro, A. J., Gorgas, J., Cardiel, N., Pedraz, S., Peletier, R. F., & Vazdekis, A. 2001b, *MNRAS*, **326**, 981
 Christlieb, N. 2003, *Rev. Mod. Astron.*, **16**, 191
 Covey, K. R., et al. 2007, *AJ*, **134**, 2398
 Fukugita, M., Ichikawa, T., Gunn, J. E., Doi, M., Shimasaku, K., & Schneider, D. P. 1996, *AJ*, **111**, 1748
 Girardi, L., Grebel, E. K., Odenkirchen, M., & Chiosi, C. 2004, *A&A*, **422**, 205
 Gratton, R. 2000, ASP Conf. Ser. 198, Stellar Clusters and Associations: Convection, Rotation, and Dynamos, ed. R. Pallavicini, G. Micela, & S. Sciortino (San Francisco, CA: ASP), 225
 Gray, R. O., & Corbally, C. J. 1994, *AJ*, **107**, 742
 Grevesse, N., & Sauval, A. J. 1998, *SSRv*, **85**, 161G
 Gunn, J. E., et al. 1998, *AJ*, **116**, 3040
 Gunn, J. E., et al. 2006, *AJ*, **131**, 2332
 Harris, W. E. 1996, *AJ*, **112**, 1487
 Hawley, S. L., et al. 2002, *AJ*, **123**, 3409
 Ivezić, Z., et al. 2008, *ApJ*, **684**, 287
 Koesterke, L., Allende Prieto, C., & Lambert, D. L. 2008, *ApJ*, in press
 Kupka, F., Piskunov, N., Ryabchikova, T. A., Stemples, H. C., & Weiss, W. W. 1999, *A&AS*, **138**, 119
 Kurucz, R. L. 1993, Kurucz CD-ROM 13, ATLAS9 Stellar Atmosphere Programs and 2 km/s grid (Cambridge, MA: SAO)
 Le Borgne, J.-F., et al. 2003, *A&A*, **402**, 433
 Lee, Y. S., et al. 2008, *AJ*, **136**, 2050 (Paper II)
 Lupton, R., et al. 2001, in ASP Conf. Ser. 238, Astronomical Data Analysis Software and Systems X, ed. F. R. Harnden, Jr., F. A. Primini, & H. E. Payne (San Francisco, CA: ASP), 269
 Morrison, H. L., et al. 2003, *AJ*, **125**, 2502
 Moultaka, J., Illovaisky, S. A., Prugniel, P., & Soubiran, C. 2004, *PASP*, **116**, 693
 Nelder, J., & Mead, R. 1965, *Comput. J.*, **7**, 308
 Pier, J. R., et al. 2003, *AJ*, **125**, 1559
 Plez, B., & Cohen, J. G. 2005, *A&A*, **434**, 1117
 Prugniel, Ph., & Soubiran, C. 2001, *A&A*, **369**, 1048
 Re Fiorentin, P., et al. 2007, *A&A*, **467**, 1373
 Reimers, D., & Wisotzki, L. 1997, *Messenger*, **88**, 14
 Sánchez-Blázquez, P., et al. 2006, *MNRAS*, **371**, 703
 Schlegel, D. J., Finkbeiner, D. P., & Davis, M. 1998, *ApJ*, **500**, 525
 Stoughton, C., et al. 2002, *AJ*, **123**, 485
 Strauss, M., & Gunn, J. E. 2001, SDSS Data Release 3, Technical Note (Baltimore, MD: STScI) <http://www.sdss.org/dr3/instruments/imager/index.html>
 Valdes, F., Gupta, R., Rose, J. A., Singh, H. P., & Bell, D. J. 2004, *ApJS*, **152**, 251
 Wilhelm, R., Beers, T., & Gray, R. 1999, *AJ*, **117**, 2308 (WBG99)
 Wisotzki, L., et al. 2000, *A&A*, **358**, 77
 Woolf, V. M., & Wallerstein, G. W. 2006, *PASP*, **118**, 218
 York, D. G., et al. 2000, *AJ*, **120**, 1579
 Zhao, C., & Newberg, H. J. 2006, arXiv:astro-ph/0612034